uOttawa

L'Université canadienne
Canada's university

FACULTÉ DES ÉTUDES SUPÉRIEURES ET POSTOCTORALES

uOttawa

L'Université canadienne
Canada's university

FACULTY OF GRADUATE AND POSDOCTORAL STUDIES

Andrew Li-Pook-Than
AUTEUR DE LA THÈSE / AUTHOR OF THESIS

M.Sc. (Physics)
GRADE / DEGREE

Department of Physics
FACULTÉ, ÉCOLE, DÉPARTEMENT / FACULTY, SCHOOL, DEPARTMENT

In *situ* Raman Spectroscopy of Carbon Nanotube Growth by Chemical Vapor Deposition

TITRE DE LA THÈSE / TITLE OF THESIS

P. Finnie
DIRECTEUR (DIRECTRICE) DE LA THÈSE / THESIS SUPERVISOR

CO-DIRECTEUR (CO-DIRECTRICE) DE LA THÈSE / THESIS CO-SUPERVISOR

M. Godin

Javier Giorgi

Kevin Graham

Gary W. Slater
Le Doyen de la Faculté des études supérieures et postdoctorales / Dean of the Faculty of Graduate and Postdoctoral Studies

In situ Raman spectroscopy of carbon nanotube growth by chemical vapor deposition

Andrew Li-Pook-Than

Thesis submitted to the
Faculty of Graduate and Postdoctoral Studies
In partial fulfillment of the requirements
For the Master of Science degree in physics

Department of Physics
University of Ottawa

Your file Votre référence
ISBN: 978-0-494-65522-1
Our file Notre référence
ISBN: 978-0-494-65522-1

TABLE OF CONTENTS:

LIST OF FIGURES:

LIST OF TABLES:

Figures 19, 20, 21, 23, 25, 26, 28, 29, B1, C1, D1, D2, D3, D4, D5, D6, and E1 reproduced in part with permission from the Journal of Physical Chemistry C, submitted for publication.

ABSTRACT

In situ Raman spectroscopy was used to track the growth of carbon nanotubes grown by chemical vapor deposition. The dynamic evolution of three kinds of Raman bands, namely the G, D, and RBM bands, was analyzed. The evolution of nanotube diameter and crystallinity was analyzed from the RBM and D/G band evolution, respectively. A characteristic growth sequence consisting of four distinct stages of growth was consistently observed. The growth rate of each stage was found to decrease with increasing temperature, possibly due to parasitic, competing reactions, and energy scales for each stage are extracted. The evolution and nanotube distribution of samples grown with and without alumina support layers is contrasted and the role of alumina is discussed.

1. MOTIVATION

Carbon nanotubes (CNTs) are "helical microtubules of graphitic carbon" [1] with unique physical properties resulting from characteristics such as their high aspect ratio, high surface area, sp^2 hybridized C-C bonds and quasi-one-dimensional electronic structure. The potential of these mechanical, electrical, optical, thermal and chemical properties for different material applications, coupled with the wide selection of currently developed synthesis and device-fabrication methods, makes them a popular research topic. Known applications range from the construction of load-bearing composite materials to field-effect transistors (FETs) to field emission displays to biochemical sensors. [2--5]

Experimental advancements have allowed CNTs to be grown in relatively high yield prior to being characterized and incorporated in devices. However, many applications would benefit from improved control over the overall structure, species purity, length, distribution, orientation and yield of synthesized CNTs. Although many studies in CNT separation and manipulation are ongoing, the fundamental problem remains in the deficiency in knowledge regarding basic growth processes and the experimental parameters that govern them. Arguably, further refinements of *in situ* data collection techniques and postulated growth models may ultimately be required before vast improvements in synthesis control and the mass production of many CNT devices can occur.

This study investigates the growth processes of CNTs grown under chemical vapor deposition (CVD). CVD is currently the most commonly used method of CNT

synthesis, due in part to its relative adaptability, low cost and usefulness in growing aligned CNTs. [2] Raman spectroscopy, the primary characterization method, is performed concurrent with growth at elevated temperatures. While room temperature Raman spectroscopy has been firmly established as a dependable means of inferring CNT structure and population distribution, the use of this technique at high temperature is more recent. [6--10] As we will show, we can reliably investigate the growth processes of different CNT samples grown at different temperatures and this provides unique insight into the fundamental stages of nanotube growth.

2. CNT STRUCTURE

2.1 Molecular structure

CNTs are an allotrope of carbon in which all atoms are sp^2 hybridized and arranged in a cylindrical configuration. The ends of these tubes may either remain open or terminate in rounded fullerene caps. CVD grown CNTs may have one end affixed to the sample surface. [4] The simplest CNTs are single-walled carbon nanotubes (SWNTs), which can be perhaps best visualized as a rolled up sheet of graphene (i.e. a single layer of graphite) as shown in Figure 1.

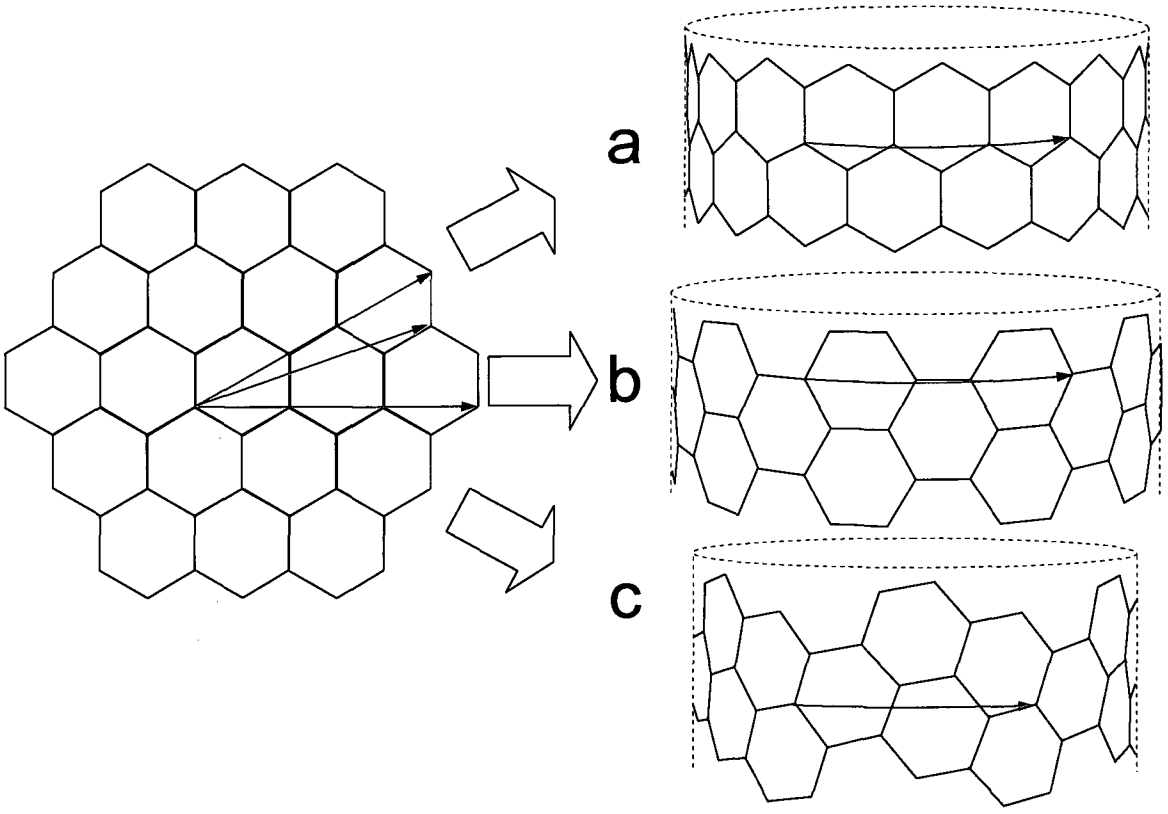

Figure 1: Examples of different SWNT structural configurations: (a) zigzag, (b) armchair, (c) chiral.

In this schematic, different SWNT structural configurations (i.e. chiralities) can be obtained depending on the direction the sheet is rolled. Initially carbon atoms are arranged in a flat honeycomb-like lattice, where the atoms are at the hexagon vertices and each hexagonal side represents a hybridized electron bond. If the rolling direction is perpendicular to any bond, the resulting SWNT structure is called "zigzag". If the direction is parallel to any bond, the SWNT is "armchair". If the direction is at any other angle, the nanotube is "chiral". One consideration important to CNT device construction is that chirality affects the electronic bandgap of each SWNT, such that armchair SWNTs are metallic, while zigzag and chiral nanotubes are either moderate-gap or very narrow-gap semiconductors. [11] For room temperature applications, these narrow-gap

semiconductors behave as metals. Experimental evidence suggests that SWNTs are usually grown without any chirality preference, which results in approximately 2/3 of all synthesized SWNTs being moderate-gap semiconductors. [12--14]

The typical diameters of synthesized SWNTs are between 0.4-5 nm [15] and roughly vary inversely with the electronic bandgap energy. [4,16,17] On a substrate, CNT orientation is typically governed by Van de Waals forces and SWNTs will often form bundles with diameters of ~10 nm. Multi-walled carbon nanotubes (MWNTs) are simply comprised of several layers of SWNTs concentrically aligned along the same axis and have corresponding larger diameters, often tens of nanometers in width. CNT length can vary tremendously and ultralong CNTs can be grown to centimeters in length. The extremely high length-to-diameter ratio of CNTs is desirable in a number of applications.

2.2 Electronic structure

The electronic density of states (DOS) of both metallic and semi-conducting CNTs are dominated by sharp van Hove singularities that are present at different energies, indicating that the electronic states occupy a discrete set of preferred energy levels. This is a direct result of the quasi-1D quantum confinement that occurs along the length of the CNT. To illustrate these singularities, the one-particle DOS of an infinitely long, box-like nanowire, is calculated using the simplified method outlined in Ref. [18] and is depicted in Figure 2.

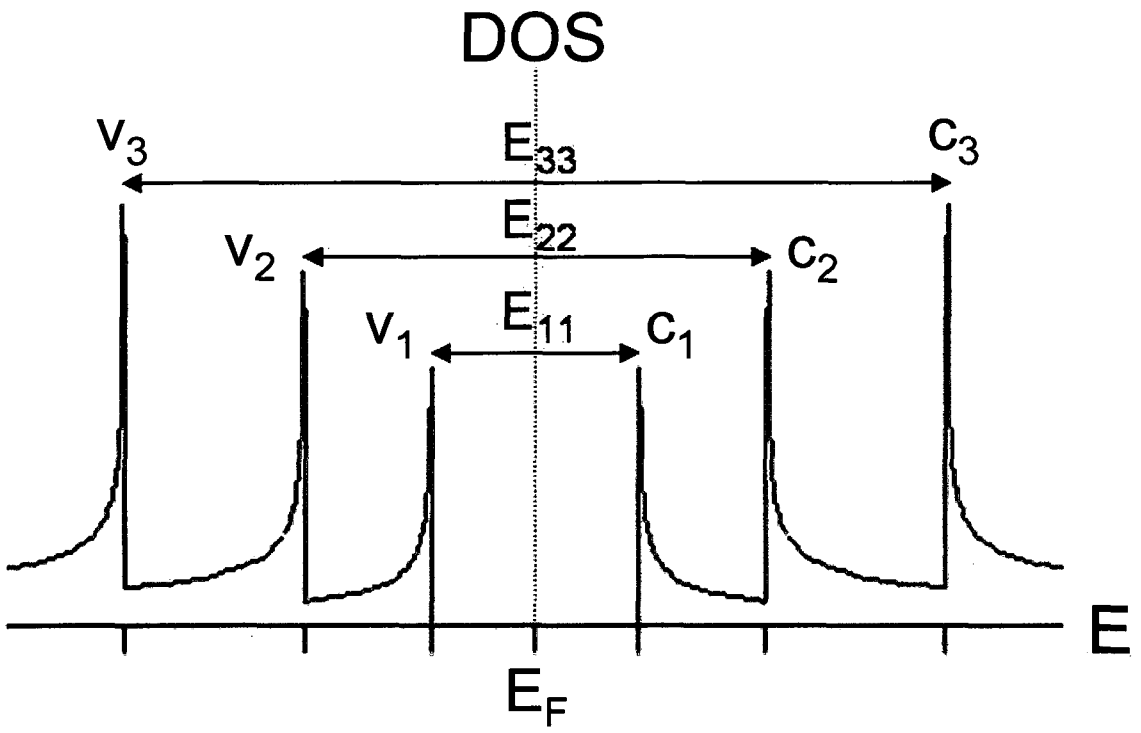

Figure 2: Schematic of the densities of states of a SWNT, calculated using the one-particle model development in ref. [18]**. See text for details.**

The boundary conditions of a SWNT more accurately correspond to a cylindrical shell than to a box, but van Hove singularities emerge in either case. Actually, this infinitely-long nanowire calculation corresponds to the familiar 2D particle-in-a-box problem with cross-sectional areas of L_x by L_y. The associated cross-sectional energy levels of this system are therefore known to be:

$$E_{i,j} = \frac{\hbar^2}{2m}\left(\left(\frac{n_x\pi}{L_x}\right)^2 + \left(\frac{n_y\pi}{L_y}\right)^2\right) \quad (1),$$

where n_x and n_y are positive integers, m is the electron mass, and $\hbar$ is the reduced Planck constant. Consequently, the 3D energy levels are:

$$E = E_{i,j} + \frac{\hbar^2 k_z^2}{2m} \quad (2),$$

where k_z is the wave vector directed along the length of the box. After some manipulation [18], we find the cross sectional DOS to be:

$$DOS_{i,j} = \frac{dN_{i,j}}{dE} = \frac{dN_{i,j}}{dk_z}\frac{dk_z}{dE} = \frac{L_z}{\pi}\left[\frac{2m}{\hbar^2(E - E_{i,j})}\right]^{1/2} \quad (3),$$

where $N_{i,j}$ is the number of states in the differential energy interval [E, E + dE]. The total DOS, as depicted in Figure 2, is given by:

$$DOS = \sum_{i,j} DOS_{i,j}(E) \quad (4).$$

In this simple, one particle, nanowire schematic, the van Hove singularities are distributed roughly symmetrically about the Fermi energy E_F. In the case of CNTs, the DOS of the E_F of a semiconductor is zero, while that of a metal is non-zero. [19] As seen in Figure 2, the singularities at negative and positive energies correspond respectively to the valence and conduction bands of the nanowire. Accordingly, each CNT of given chirality/diameter can undergo a specific set of optical transitions when exposed to incoming light, such that the transitions are most probable between the singularities. In other words, each metallic or semiconducting CNT can be defined by a set of energy transitions E_{ii}, and can be characterized by optical techniques that probe the energy difference between singularities, such as photoluminescence or resonance Raman spectroscopy.

A more accurate and refined explanation can be given in terms of bound electron-hole pairs known as excitons, which are expected to develop in confined, low-

dimensional systems [17,20]. The excitonic DOS is qualitatively similar to the E>0 portion of Figure 2, but the singularities correspond to excitonic transitions instead of interband transitions [17]. Allowable transitions can be determined theoretically by a number of so-called selection rules, such that E_{11} and E_{22} excitons can be produced, in addition to cross-transitional excitons, such as E_{12} [21]. When an optical transition such as the one in Figure 6 (see below) is initiated, an electron will be promoted to an excited state, leaving behind a hole. The electron and hole will feel a strong attraction and the exciton that forms will mediate the scattering process. Additional interactions between multiple excitons predicted by theory can lead to many-body effects that can modify optical spectra. [17,19,20,22--24] One important consequence is that the lowest optical transition of a CNT (i.e. E_{11} in Figure 2) is no longer equivalent to the electronic bandgap, although its inverse relationship with diameter remains valid. [17,24--26].

3. CVD GROWTH THEORY AND METHOD

3.1 Introduction to CVD

CVD is a high yield, adaptable process for producing CNTs of different chiralities and orientations, which can subsequently be tailored for specific industrial applications. Numerous CVD variants exist and CNTs can be grown and individually incorporated directly on different devices or, alternatively, grown in bulk before being separated and manipulated for subsequent use. For electronic devices, a wafer of doped Si with a SiO_2 buffer layer might be used as a growth base, while powders or specialized substrates are more appropriate in other cases. [15] The synthesized CNTs will generally fall into two

categories, namely: vertically-aligned nanotube arrays (i.e. forests) that grow away from the sample surface, or surface nanotubes that grow along the horizontal surface plane.

Three key components are typically involved in CVD-CNT precipitation: (1) catalyst nanoparticles, (2) high growth temperatures, and (3) a carbon source. We now consider these requirements in greater detail.

Catalyst nanoparticles assist the formation of CNTs in large numbers, and can be pre-deposited or coated on the sample prior to growth. Depending on the particular growth temperature and carbon diffusion processes at work [15], nanoparticles are typically thought to become saturated with carbon prior to CNT formation, and may either actively decompose the gas molecules or simply serve as a growth template. Typical formulations are composed of transition metals, such as Fe, Co or Ni, which may either be used as pure metals or in combination with other elements (e.g. bimetallic with Mo), although other formulations are also possible [15]. Non-metallic catalysts are also possible. Catalyst nanoparticles may lie directly on the substrate surface or may lie atop an intermediate layer of support material, which may affect such factors as CNT yield and diameter. [15]

CVD is performed at only moderately high temperatures typically between 600-1000°C. The reactor is described as "hot-walled" if the reactor wall is heated to a temperature that is the same or comparable to that of the sample during growth; otherwise, if only the sample is heated, it is "cold-walled" [14]. Depending on the heater geometry, hot-walled heating may increase the decomposition rates of the carbon feedstock gas and produce higher yields of lower quality CNTs compared to cold-wall heating. [27]

Finally, a carbon-carrying source gas/vapor must be controllably introduced into the heated growth system, typically alongside H_2 gas, for growth to occur. Common reactants include CO, CH_4, C_2H_4, C_2H_4 and C_2H_5OH. [15,28] At elevated temperatures, CNTs will burn in the presence of O_2. Growth is therefore performed in enclosed reactors and gas content is typically controlled by process gases, such as Ar. These typically inert gases are used to purge the reactor and control the duration of the growth process, while sometimes acting as gas carriers. [2,15]

Numerous factors can influence the final outcome of CNT CVD growth and, evidently, modifications to fundamental growth parameters, such as growth temperature, catalyst preparation/support, gas pressure or gas flow rate/direction, will typically impact important factors like CNT purity, population distribution, yield, orientation, and the overall reactivity of the process. Extra process steps may also be required to optimize growth. For example, preheating the sample prior to growth may affect catalyst particle size or result in the oxidation/reduction of the catalyst, and thus affect CNT yield. The presence of just one extra chemical mediator can also have a large effect on synthesis. For instance, in certain CVD applications, such as for the growth of ultralong, surface or forest CNTs [28,29], a controlled amount of water vapor has been found to substantially prolong catalyst activity. [28,30,31] In our present study, we make use of the finding that alumina-oxide catalyst supports have been found to promote high density, forest growth. [32--34] Other more general physical parameters, such as the sample lithography, or the electric/magnetic field across a sample, can also be modified to affect growth.

3.2 CVD growth theory

While a general description of CVD-CNT growth is widely accepted, the specific chemical steps behind this universal growth process are still not fully understood. Regardless of CNT length or orientation, SWNT diameter is widely believed to correlate directly with nanoparticle diameter. It is generally thought that each SWNT requires a nanoparticle to form around at the onset of growth; see, for example, refs. [35--38]. Studies (e.g. [39]) also suggest that the outer-diameter of MWNTs will also match nanoparticle size.

It is also well established that growth can proceed in one of two ways depending on which particular growth method and temperature are used and how the catalyst nanoparticle (frequently a metal, i.e. ref. [40]) behaves during the initial formation (i.e. nucleation) of the nanotube. [15] In "surface carbon diffusion", impinging carbon-source molecules break down and nucleate the exposure surface of each nanoparticle. As more molecules break down, saturating the surface, the emerging CNT will lengthen. Alternatively, in "bulk carbon diffusion", carbon-source molecules may decompose and enter the catalyst nanoparticle to form complexes. Only once the entire nanoparticle is saturated with enough carbon will a solid CNT begin to form and lengthen, while the catalyst continues to dissolve new carbon molecules. The nanoparticle may either be in solid or liquid phase under both diffusion processes. [15] The underlying substrate is typically assumed to remain inert throughout the growth process, although certain types of substrate may have more active roles.

As the CNT lengthens, depending on the substrate or catalyst-support material, the catalyst nanoparticle may remain fixed on the surface or may detach and form the tip of the growing nanotube, in what is respectively known as either base- or tip-growth, depicted schematically in Figure 3. Growth appears to occur in a functionally similar manner in both cases. [15]

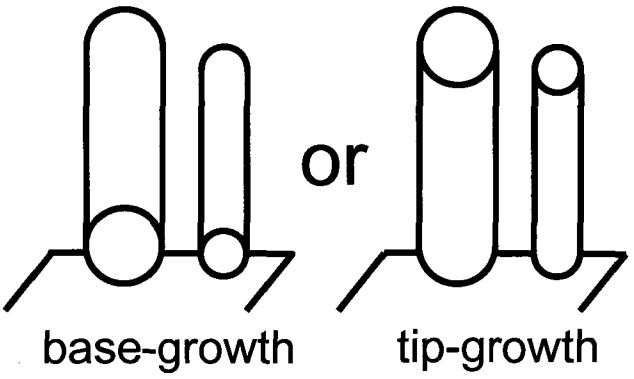

Figure 3: Schematic contrasting base- and tip-growth for two vertically aligned CNTs.

CNTs will tend to grow straight, but can bend if any defects form on their sidewalls, if they make contact with an obstacle, or if they are otherwise pushed or pulled by an external force. Depending on their length and number, surface CNTs tend to be straight, while vertical forests, especially shorter ones, may tangle at different heights. Additionally, experimental factors like horizontally aligned gas flow, substrates of particular crystalline structure or external fields can produce extremely well aligned, straight surface tubes. Alternatively, proper substrate choice can be used to make the CNT bend in a predictable manner [41].

In the case of ultra long CNT synthesis, growth may continue indefinitely and be restricted only by substrate length. However, for lower yield synthesis, the CVD-CNT growth rate will typically eventually decrease and fall to zero. This growth termination is

usually attributed to so-called "catalyst poisoning", whereby the gradual formation of amorphous carbon or a dense graphitic shell over the catalyst nanoparticle effectively prevents new carbon-source molecules from making contact with the nanoparticle [42]. In the case of ultra long, aligned surface CNT growth, the amount of van der Waals attraction between the substrate and the growing CNT may affect the rate of catalyst poisoning or other growth inhibiting surface interactions [15].

3.3. Growth substrates

We chose to analyze growth on two types of substrate material known to generate significantly different yields and distributions of CNTs under CVD. The CNT growth spectra obtained both substrates was different and could be compared against each other at given growth temperatures. All substrates were prepared at IMS-NRC. A structural schematic is presented in Figure 4.

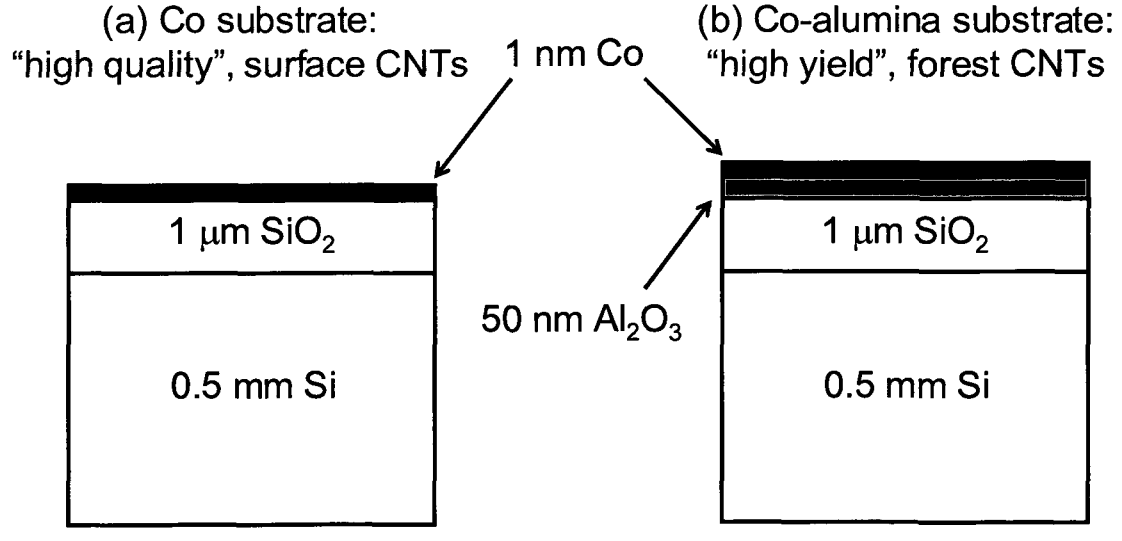

Figure 4: Schematic cross-section of the two utilized substrates: type (a) cobalt substrate and type (b) cobalt-alumina substrate.

The same base layer is found in both substrates; it consists of a 0.5 mm thick undoped Si block topped with a 1 μm thermally generated SiO_2 layer. A 50 nm alumina catalyst support layer is electron beam evaporated over *one* of the substrates, while both substrates are topped with a 1 nm Co metal catalyst layer, upon which grow the CNTs. All samples are hand-cleaved from the substrate material to surface dimensions of ~2.5mm × 4mm to fit the reactor vessel. For simplicity, samples containing or not containing the alumina layer will be referred to respectively as "Co-alumina samples" or "Co samples".

The Co samples typically produced lower yield, higher quality CNTs compared to the Co-alumina samples. As we shall show, GRI and SEM images reveal networks of surface-aligned CNTs of varying density, while Raman spectra indicate the presence of high crystallinity CNTs and many SWNTs of different chiralities at room temperature.

By contrast, the Co-alumina substrate typically produced higher yield, lower quality samples. Tall, vertically-aligned CNT forests at least several microns in height are commonly observed in these samples under SEM. Spectral features denoting numerous low crystallinity CNTs are typical. Raman peaks indicating the presence of SWNTs in the Co samples instead appear to be either absent or at significantly lower intensities in the Co-alumina samples at equivalent growth temperatures.

3.4. CVD apparatus and growth method

Two important factors that affect CNT-CVD growth are: (1) the temperature of the sample and (2) gas composition during growth. In our study we systematically vary the growth temperature for each substrate type, but maintain the same gas conditions (i.e. chamber pressure, flow rate) from experiment to experiment. To establish control over these two factors, all samples were grown under the same hot wall CVD system, schematically illustrated in Figure 5.

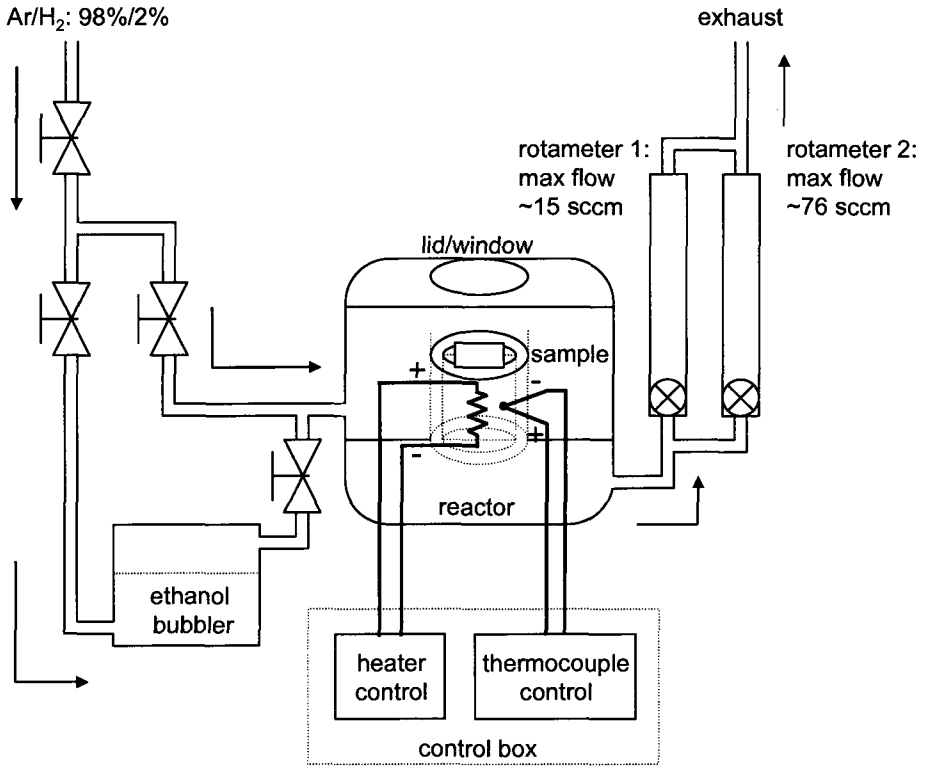

Figure 5: Schematic of the utilized CVD reactor and flow control system.

The sample temperature is controlled by the heater of our commercial cell reactor (Linkam Model CCR 1000).The reactor has a volume of roughly 80 cm^3 and has a lid and window for optical measurements. The thermo-electric heater body consists of a hollow, ceramic cylinder that gas can pass through, upon which the cleaved sample is typically centered. When loading a sample, the reactor is opened and the sample is placed facing up atop the cylinder. A ceramic half-disc placed on the lower half of the sample holds it in place. The heater temperature is monitored at all times by a thermocouple relayed to a control box/computer system. This system also regulates power input to the heater, so the heater temperature can either be fixed at set values or increased/decreased at controllable ramping rates.

A separate flow control system regulates gas exposure over the sample. We use an Ar/H_2 mix (98%/2%) as a carrier/purging gas and anhydrous liquid ethanol as a carbon precursor. Using a series of valves, the carrier gas can be made to flow through an ethanol filled bubbler to the reactor or, alternatively, directly to the reactor, thereby bypassing the bubbler. All gas entering the reactor is directed over the sample surface and through the cylinder, before exiting. Two parallel rotameters that are connected downstream to the reactor allow flow rates of up to ~15 sccm and ~76 sccm, and can be simultaneously or independently opened to the exhaust.

The same basic growth procedure is used for all samples and is performed concurrently while collecting spectral data. Once the sample is loaded and the reactor is sealed, the gas system is purged out for 20 minutes with Ar/H_2 at maximum flow. This is done to remove O_2, which burns CNTs at high temperatures, any unwanted ambient carbon-precursor gases (e.g. CO_2), and any other reactive gases that might interfere with

the CVD process. The purge is done at 200°C to ensure that any trace amounts of ethanol from previous experiments are flushed out in vapor form. Afterwards, the heater is brought to the desired growth temperature (from 675°C – 875°C). The flow rate is reduced to 2 sccm, a relatively low value that was found to produce CNT growth with relative strong spectral signals on the Co samples, and the bubbler is opened. Ethanol will then reach the sample causing CNTs to be formed. The bubbler is left opened for 20 minutes for the Co samples and for only 5 minutes for the Co-alumina samples, with the latter samples already producing excessive CNT yields during this short time. Finally, with the bubbler closed off, the reactor is purged out for 5 minutes at maximum flow rate before being cooled back down to room temperature. The step-by-step process is presented in the Appendix A.

4. RAMAN TECHNIQUES AND METHOD

4.1 Raman scattering theory

Raman spectroscopy consists of a family of characterization techniques that are commonly used to analyze the molecular structure of different media by probing the vibrational states of bonded atoms. [43] These techniques exploit the inelastic, nonlinear optical phenomenon known as Raman scattering. The most general case of Stokes Raman scattering is schematically depicted in Figure 6.

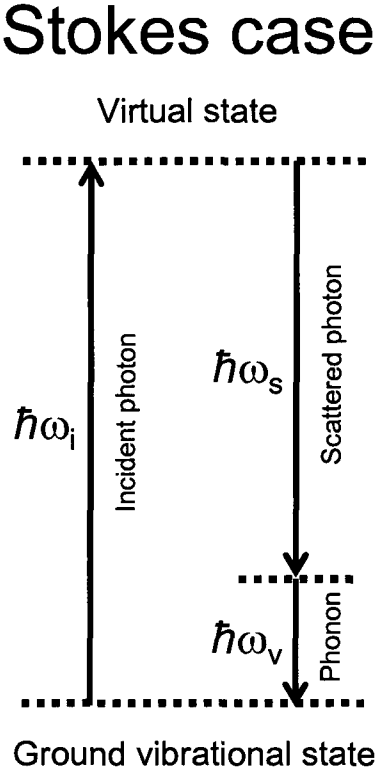

Figure 6: Schematic of Raman scattering of a Stokes-shifted outgoing photon.

High intensity (typically laser) incident light is sent towards the target medium with photon energy $\hbar\omega_i$. Some of these photons will each excite a molecule from its ground state to a higher energy virtual state, causing an optical phonon of energy $\hbar\omega_v$ to be emitted. The photon itself will then scatter away with reduced energy $\hbar\omega_s$. By conservation of energy, we obtain:

$$\hbar\omega_s = \hbar\omega_i - \hbar\omega_v \qquad (5)$$

Depending on the specific DOS of the target, different phonon energies and associated vibrational states are produced, which in turn determine the energy of the scattered photons. These photon energies can be recorded with the spectrometry system and structural information from the resulting spectra can then be inferred. Although Figure 6

depicts the case of one phonon produced during scattering, multiple phonon events are also possible. [19]

Anti-Stokes scattering (not shown) is similar to Stokes scattering, the main difference being that at the same moment the molecule absorbs the incident photon, it also absorbs a pre-existing phonon of energy $\hbar\omega_v$. [43] The scattered photon then leaves with the additional energy. Because the population of molecules with initial energy $\hbar\omega_v$ is low at lower temperatures, the scattered anti-Stokes photon signal intensity is substantially lower than the Stokes signal and is less commonly analyzed, unless it is otherwise enhanced. In our particular apparatus, the Stokes signal was accessible due to our use of a long wave pass, ultra steep edge filter. This filter allowed longer wavelength, Stokes scattered photons to reach the spectrometer, and blocked both the laser line and the shorter wavelength, anti-Stokes photons.

4.2 CNT resonant Raman spectra

The Raman spectra of a CNT sample is dependent on the vibrational states, and therefore on the diameter and chirality of the nanotubes from which optical photons are scattered. [16,19,21,26] The sample environment and physical/chemical effects, such as CNT doping, can also affect the spectra in different ways. [44] For the purpose of background comparison, Figure 7 contrasts the Stokes shifted spectra of a typical sample without any CNTs (in red), against its spectra after CNTs have been grown on it (in black). Substrate related features are indicated with asterisks. The Raman shift, corresponding to $\Delta E = \hbar\omega_v$, is presented in wavenumbers in units of cm^{-1}, where 1 cm^{-1} =

1.240×10^{-4} eV. As mentioned, the high intensity Rayleigh peak, corresponding to elastic scattering at $\Delta E = 0$, has been filtered out.

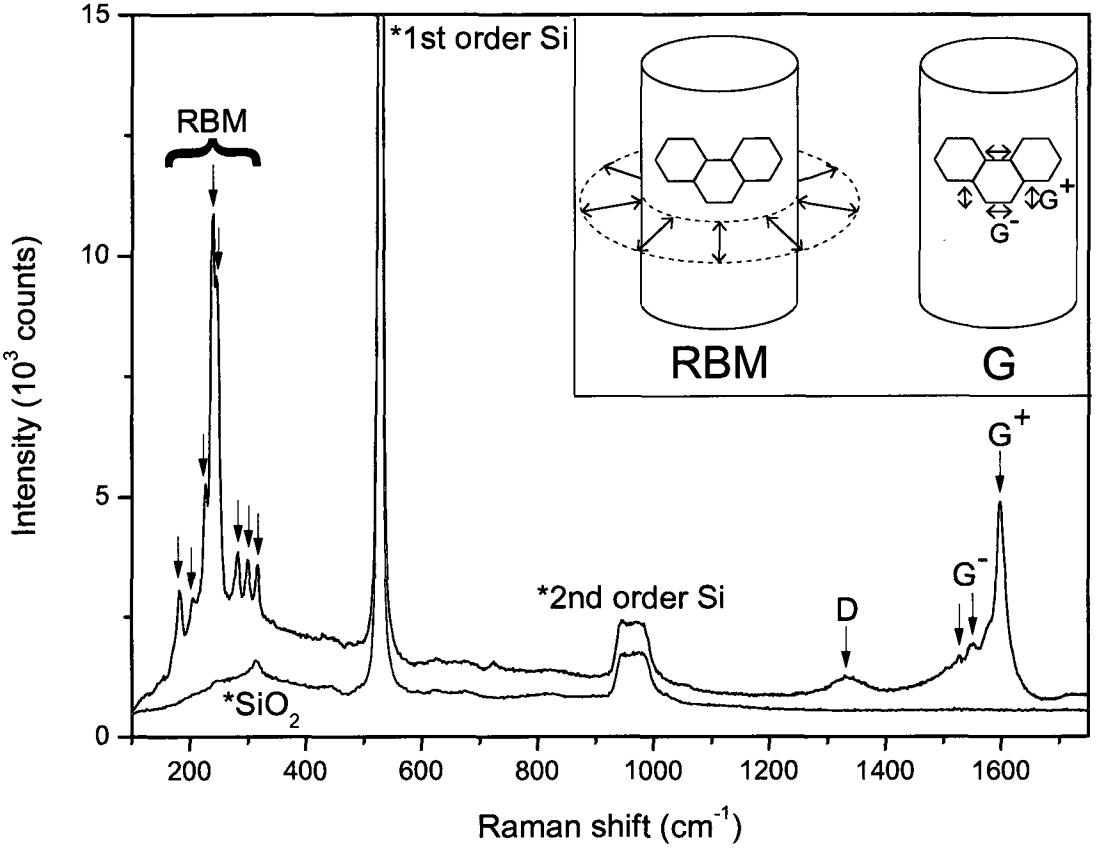

Figure 7: Typical pre-growth (red) and post-growth (black) Raman spectra of a CNT sample. The vibrational modes associated with the RBM and G bands are depicted in the inset. The G+ and G- bands correspond to perpendicular directions of G band vibration. The asterisks indicate spectral features that originate from the Si/SiO_2 substrate. Black arrows indicate CNT-related peaks.

The radial breathing modes (RBMs) are a series of peaks from approximately 100-400 cm^{-1} that are a spectral signature of SWNTs. As depicted in the inset of Figure 7, a RBM peak corresponds to the optical phonon associated with the radial, in-phase expansion and contraction of constituent SWNT carbon atoms. [19] It is well established that RBM peak frequency is roughly inversely proportional to SWNT diameter, with peaks at increasing higher wavenumbers corresponding to progressively smaller diameter

nanotubes. The individual layers of thin MWNTs may also contribute to the RBM. [16,45]

In practice, only SWNT populations (or thin MWNT walls) that are resonant (or near-resonant) with the incident or scattered photon frequency can produce scattered RBM signals that are enhanced enough to be detected. The Raman spectroscopy of CNTs is therefore a form of resonance Raman spectroscopy (RRS). It is common practice to choose a particular incident photon (i.e. laser) frequency, with the intention that it matches the resonance condition of a (hopefully representative) set of CNT species. In terms of Figures 2 and 6, this means that one can choose the laser energy $E_{LASER} = \hbar\omega_i$ to overlap with a given optical transition E_{ii}, such that either $\hbar\omega_i = E_{ii}$ or $\hbar\omega_i = E_{ii} + \hbar\omega_v$. Additionally, one can analyze a single CNT sample with different (i.e. tunable) laser frequencies, resulting in SWNTs of different chiralities and diameters appearing in each separate spectrum.

The G band, located between ~1500-1600 cm^{-1}, is another Raman band important for CNT analysis. It indicates the presence of sp^2 hybridized C-C bonds (found in graphite, SWNTs and MWNTs) and in the case of CNTs, as depicted in the inset of Figure 7, it is the result of tangential vibrational modes along the nanotube surface [16]. These optical phonon modes can either be longitudinal (LO) along the length of the CNT or transverse (TO) along its circumference. These modes split the G band into two components, namely, a high intensity peak at ~1600 cm^{-1} called the G+ (from the LO mode), and one or more lower intensity peaks from 1500-1575 cm^{-1} called the G- (from the TO mode). [19] The lower G- frequency is sensitive to CNT curvature, and G- peaks originating from semiconducting CNTs will generate different lineshapes than those of

metallic CNTs. [19] It follows that if only planar graphitic bonds are present, then only one G component will be visible. [19] Multiple G- peaks can sometimes indicate the presence of different SWNT diameters. [16,19]

Sometimes an isolated SWNT can be spectrally analyzed. In such cases, the G- will be at a higher wavenumber and at a weaker intensity for a semiconducting SWNT than for a metallic SWNT, and the G band will thus appear more asymmetrically split. This amount of splitting in both semi-conducting and metallic CNTs increases as $1/d_t^2$ increases, where d_t is the nanotube diameter. [19,44]

The broad D band is located at ~1350 cm^{-1} and is indicative of a break in the symmetry of the sp^2 C-C bond lattice of graphitic carbon (i.e. disorder)[44], which indicates some sp^3 bonding character. Thus, the I_D/I_G signal intensity ratio is frequently used to quantify how many structural defects/impurities are present in the analyzed CNT population; samples with high crystallinity will exhibit low I_D/I_G ratios and vice-versa. For instance, the post-growth spectral data in Figure 5 has $I_D/I_G \approx 0.11$ which is a relatively low value, typical of a Co sample. Co-alumina samples grown at the same temperatures, by contrast, will tend to exhibit much larger I_D/I_G ratios.

In this study, we restrict our analysis to the RBM, G and D bands from 150-1750 cm^{-1}. Other CNT-related Raman bands are typically less well studied and, among our samples, are often of weaker spectral intensity. These include the sample dependent intermediate-frequency modes (IFMs) located between ~500-1000 cm^{-1}, and the second-order M band and iTOLA modes located between ~1700-1900 cm^{-1}. [19,44] An overtone of the D band, known as the G' band, is located around 2600 cm^{-1} and can be useful in determining graphene layer number and studying CNT crystallinity. [44]

4.3 SWNT diameter calculation and Kataura plots

Once the wavenumber of an RBM peak has been identified, the diameter of the corresponding resonant SWNT species can be calculated. The relationship is of the form:

$$\omega_{RBM} = \frac{a}{d_t} + b \quad (6)$$

where ω_{RBM} is the RBM peak wavenumber, and a and b are constants that depend on the SWNT orientation and spectral environment, with typical values that range from a~210-250 cm^{-1}·nm and b~0-20 cm^{-1}. [16,19,26] The values of a and b are generally obtained through previous characterization experiments and are dependent on factors such as whether the CNTs are bundled, or whether they are suspended in solution or lying atop oxidized substrate.

Experimental and theoretical data relating the resonance energies of different semiconducting and metallic SWNTs species to their diameters are frequently plotted in what are widely known as Kataura plots. [46--51] A schematic of a Kataura plot is shown in Fig. 8, based on ref. [52]. Different excitable semiconducting (black dots) and metallic (red circles) SWNTs are found to be detectable at only certain optical transitions and SWNT diameters.

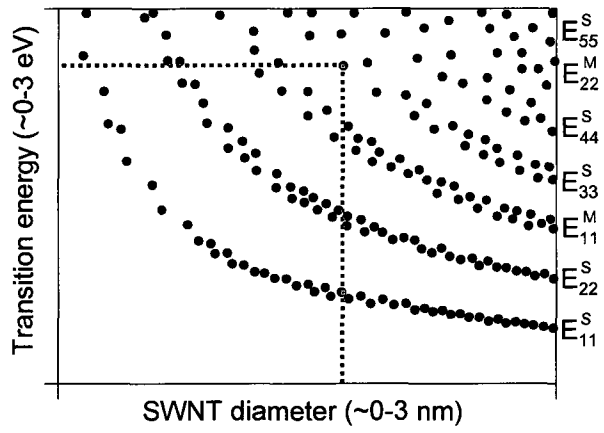

Figure 8: Kataura plot schematic, based on ref. [52]. Excitable semiconducting (black dots) and metallic (red circles) SWNTs are indicated for different RRS optical transition energies. The resonant E^S_{33} optical transition for one particular SWNT of known chirality is indicated, where the green dotted lines intersect.

Because the transition energy E_{ii} is determined by the laser and because SWNT diameters can be calculated from Equation 6, the chirality of resonant SWNT species can be identified from an accurate Kataura plot. This is schematically depicted in Figure 8 by the intersecting, green lines. A single 532 nm (i.e. 2.33 eV) laser was used in the present study. In other studies, multiple laser frequencies are frequently used to probe different chiral CNT populations over a range of transition energies.

4.4 Global Raman imaging of CNTs

Global Raman imaging (GRI) is an imaging technique closely related to RRS, a variant of which was developed for the imaging of CNTs at NRC-IMS. [53,54] Essentially, the Raman signal scattered from a CNT sample can be passed through a microscope objective and filtered of all but a small range of signal energies, before being sent to a CCD camera. The two-dimensional plan view signal distribution can thus be

recorded, allowing one to take snapshots or create time-dependent movies of focused sample region. If the unfiltered region contains the G band then, under the right optical conditions, the growth of CNTs and other forms of graphitic carbon can be recorded. Additionally, by splitting the signal prior to filtering, the GRI image can be monitored concurrently with the Raman spectra.

A GRI snapshot of an isolated, clearly visible surface SWNT (or possibly a thin SWNT bundle) grown from an off-screen catalyst deposition is shown in Figure 9. This sample was not grown in the current study. In the case of substrates with lithographically produced trenches, CNTs that grew suspended over the trenches were also clearly visible, due to their enhanced Raman signals. [53--56]

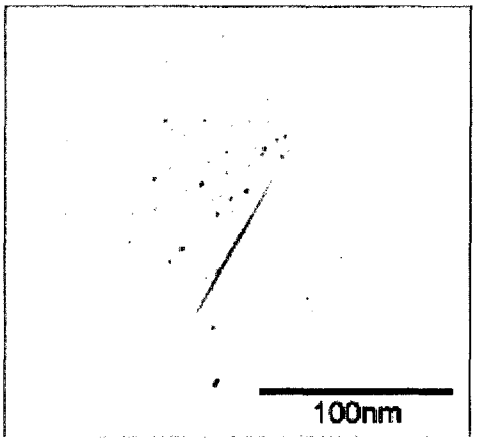

Figure 9: GRI image of an isolated SWNT (or thin SWNT bundle) with inverted image brightness.

In this study, due to the uniform catalyst deposition and growth conditions that were used, no individual CNTs could be resolved or tracked during growth. CNT growth was instead visible as a gradual increase in overall brightness on the given imaged region, subject to fluctuations in the spectral background. GRI was therefore primarily used to

focus the incident beam at a particular sample region prior to CNT growth and to ensure that the spectroscopically analyzed region is representative of the entire sample.

4.5 Optical apparatus

Raman spectra and GRI monitoring were performed concurrently using a single optical apparatus. This apparatus, schematically depicted in Figure 10, was operated independently from the CVD growth setup, and was previously used in refs. [53], [54], and [57].

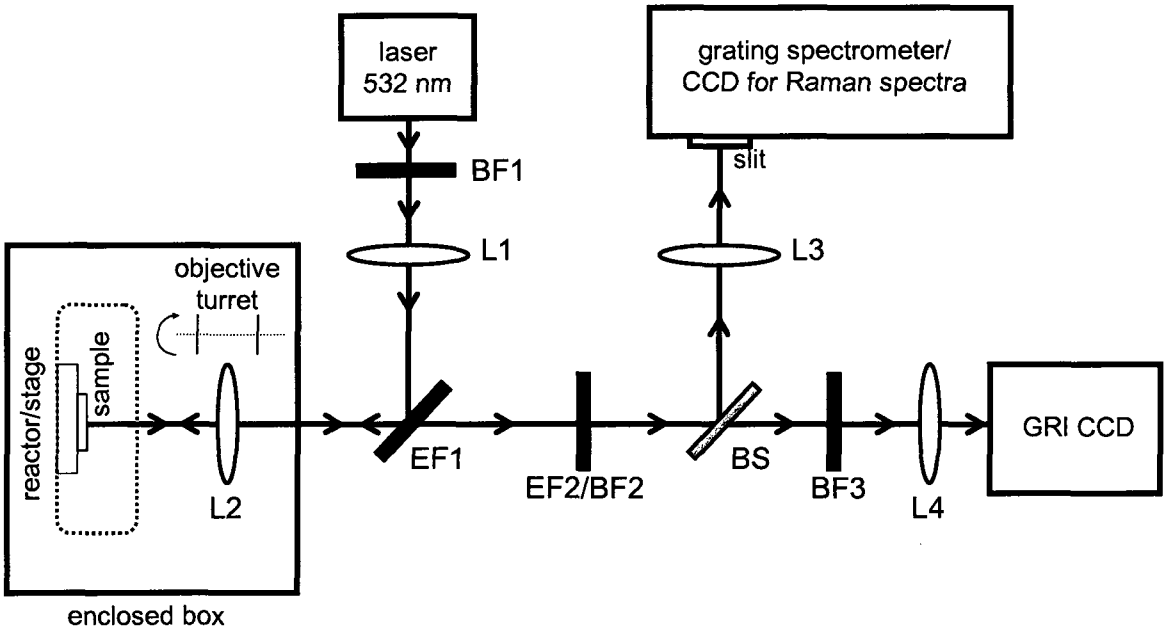

Figure 10: Schematic of the combined resonance Raman spectroscopy/global Raman imaging apparatus.

The spectral monitoring of samples is as follows. Light from a 532 laser source, with ~0.3W of incident power, is first sent through a matching laser line band pass filter (BF1) to clean the signal frequency. To reduce the effect of localized laser heating on the

sample surface and to increase the laser spot size on the sample, the laser also passes through a defocusing lens (L1). A long wave pass, ultra steep edge filter (EF1) then transmits the beam through one of several turret-mounted microscope objectives (L2), before striking the sample. A 20× long working distance microscope objective (with 0.6 numerical aperture) was used for all our samples and the resulting power density of the defocused laser spot on a given sample surface was ~30 $\mu W/\mu m^2$.

At this point, the sample has already been loaded in the vertically-mounted CVD reactor. The reactor can be translated laterally or parallel to the incident beam, such that it may be centered and focused as required. An alternative, open-air stage is also available for the *ex situ* analysis of pre-grown samples.

The scattered signal is collected back through L2, and passes through EF1. As mentioned, the Rayleigh and anti-Stokes signals are filtered out, allowing only the Stokes signal to pass. The beam then passes through additional edge and band pass filters (EF2/BF2) in order to cut its intensity and to further clean out any remaining Rayleigh signal, before encountering a beam splitter (BS).

One arm of the BS transmits a portion of the beam through a focusing lens (L3) on to the 100 μm slit of a 0.25 m grating spectrometer. A 1200 line/mm grating was used for all samples and the spectra is captured and recorded by a thermoelectrically (TE) cooled CCD.

The other arm sends the signal through a band pass filter (BF3) that matches with the G band and part of the D band. It is then focused through a focusing lens (L4) and the plan view image is captured and processed by a second CCD for GRI monitoring.

4.6 Spectral data extraction

The appearance and subsequent intensity evolution of the RBM, G and D bands concurrent to CVD-CNT growth was used as the primary CNT characterization method for all analyzed Co and Co-alumina samples. After centering and focusing a given sample, spectra were taken in the wavenumber range of 150-1750 cm^{-1}, as was done for Figure 7.

Kinetic *in situ* spectra were continuously recorded for the length of time that the ethanol bubbler was kept open, during which CNT growth occurs; that is, 20 minutes for the Co samples and 5 minutes for the Co-alumina samples. For these recordings, a 5 second integration time was used for all Co samples, and a 0.7 second integration time was used for all Co-alumina samples. One reason for the longer integration time being needed for the Co samples was because the G and D band signal intensity was typically weaker than those of the Co-alumina samples, due to lower overall CNT yield.

For comparison, pre- and post-growth spectral snapshots are also taken for each sample, at both room temperature and the synthesis temperature. These spectra were taken with an exposure time of 15 seconds. Because of the longer exposure time, the signal/noise ratio of these spectral snapshots is higher than for each snapshot during actual growth.

If a given Raman band is sufficiently intense and well separated from other bands, the spectral area beneath the band can be tracked with time. Therefore, whenever possible, the evolution of the spectral weight in the G band (centered at ~1570 cm^{-1} at growth temperatures), D band (centered at ~1325 cm^{-1} at growth temperatures) and two

distinct RBM bands (centered at ~197 cm^{-1} and ~277 cm^{-1} at growth temperatures) were analyzed.

The Si/SiO_2 spectral background below the given band must evidently first be removed for the Raman area evolution to be meaningful. The background subtraction is typically easier to perform below the wider, well-separated G and D bands, and more difficult to perform for individual RBMs, due to their generally lower intensity, poor-separation and the non-flat shape of the spectral background in this wavenumber range. The applied background subtraction method is summarized in Appendix B and was performed consistently for all analyzed Raman bands.

Before discussing our results, it is important to mention that heating the sample to our growth temperatures (from 675°C – 875°C) will modify the spectra in two major ways. First, as temperature (T) increases, the amount of black body radiation, and therefore the number of detected counts, from the substrate will increase. In particular, the integrated blackbody intensity is expected to scale with T^4. This effect can make data extraction more difficult and becomes more prominent at higher wavenumbers within our particular spectral window (from 150-1750 cm^{-1}).

Secondly, increasing temperature can alter the G, D and RBM spectra, by causing peak locations to shift and causing the intensity of different RBM peaks to change. Altering the sample temperature will also modify the energy at which the CNTs are resonant. These phenomena are discussed more fully in Appendix C.

5. SCANNING ELECTRON MICROSCOPY

Scanning electron microscopy (SEM) allows the imaging of CNTs and other nanometer-wide objects under a high magnification and depth of focus. A simplified schematic is shown in Figure 11.

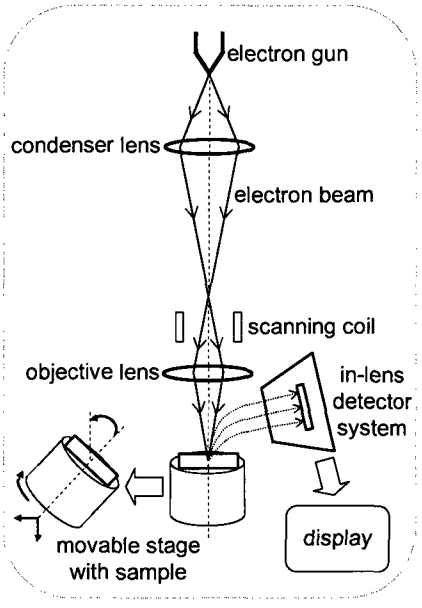

Figure 11: Scanning electron microscope schematic, adapted from refs. [58] **and** [59]

The sample lies on a stage, which may be translated horizontally, rotated, or titled vertically, within an evacuated chamber. An electron gun sends an electron beam through a series of magnetic lenses, which control the beam focus prior to striking the sample surface. As the beam is scanned across the region to be imaged (via the scanning coil), the emission of electrons originating from the surface is induced. These so-called "secondary electrons" are sent to a detector and associated lens system. Within the detector, a scintillator responds by generating photons that eventually produce an amplified electric signal that is converted into a regularly updating plan view image in the

display unit. The image magnification can be controlled by modifying the distance the electron beam is scanned. Furthermore, to examine very small objects close to the sample surface, such as nanoparticles, the sample penetration depth may be increased by increasing the beam's acceleration voltage. [58]

SEM imaging is useful for directly visualizing CNT ensembles. If a CNT is grown on and makes direct contact with an insulating surface, most commonly SiO_2, a CNT imaged under SEM will commonly experience a charging effect, resulting in increased CNT brightness. [60--64] Such CNTs will conduct surface charges that change secondary electron yield in the vicinity of the CNTs. A typical SEM image comparing charged and uncharged surface CNTs is given in Figure 12.

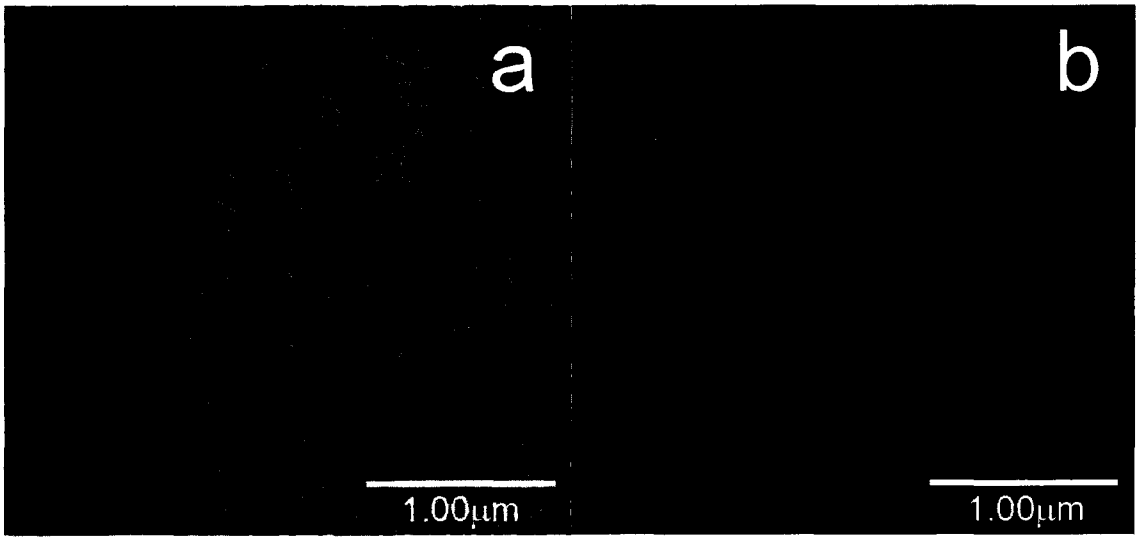

Figure 12: Plan view SEM images of surface CNTs, probably individual SWNTs, taken from the same sample at 1 kV acceleration voltage: (a) charged CNTs; (b) uncharged CNTs.

The white strands in Figure 12 (a) are surface CNTs, which appear wider than they actually are due to charging. The individual uncharged CNTs in Figure 12 (b), which probably lie atop a thick mat of CNTs/graphitic carbon, are thinner and less bright than in

(a). CNTs in different configurations (e.g. suspended CNTs, CNT forests) can experience different electrostatic/imaging effects.

6 RESULTS AND DISCUSSION

6.1 Co sample spectral evolution

The spectral evolution of 14 Co samples, grown from 675°C – 875°C was analyzed. These samples are discussed in refs.[57] and [65]. G bands of differing intensities emerged at all growth temperatures, although the intensity of the D band and the spectral weight of the RBM were found to be strongly temperature dependent. As an example, kinetic data from a typical sample grown at 725°C, a representative low temperature sample, is presented in Figure 13. [57]

Figure 13 shows the changing Raman spectra concurrent to CNT growth in 5 second intervals. The time sequence proceeds from bottom to top from t=0s, corresponding to the time the ethanol bubbler is opened, to t=250s, after which little spectral change occurs. Each individual frame is exposed for 5 seconds.

Initially, the spectra only begins to change after the t=30s frame (highlighted in green). Given the apparatus geometry, this time likely corresponds, as least in part, to the travel time required for the ethanol vapor to reach the sample surface, which will be a factor in virtually any kind of CVD growth. Because the gas flow apparatus remains

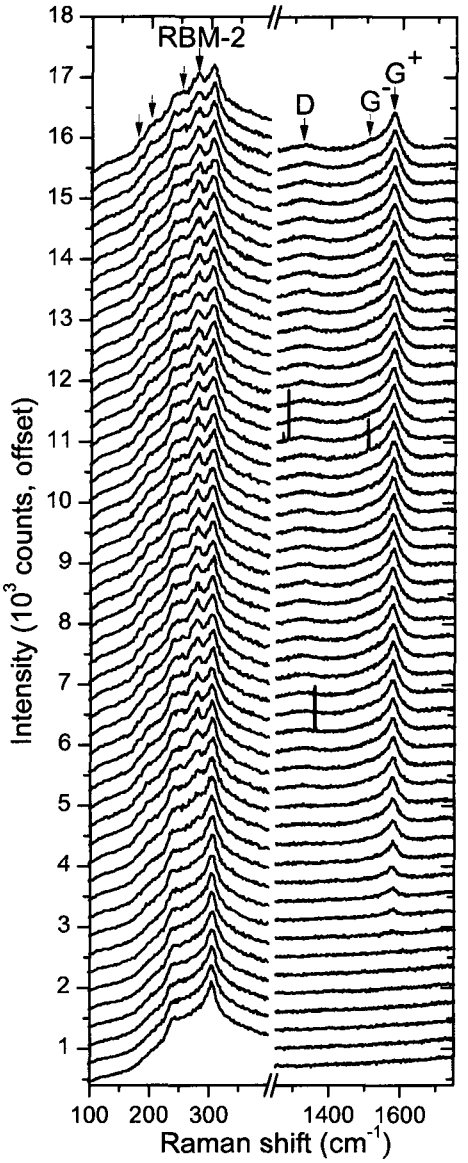

Figure 13: Kinetic Raman spectra from the Co sample grown at 725°C. The spectra from t=0s (bottom frame) to t=250s (top frame) is presented in intervals of 5 seconds, with an individual frame exposure of 5 seconds. Black arrows indicate high intensity, well separated Raman bands. Gray arrows indicate low intensity and/or poor resolved bands. Adapted from ref. [57].

unmodified in all growth runs, this travel time is expected to be the same for all samples. Actually, among all the analyzed samples, 30 seconds was found to be the shortest delay time required before detectable G, D and RBM band emergence. In particular, only those

Co samples grown below 800°C experienced this minimum growth delay, to within a 5 second error. Somewhat surprisingly, other samples experienced longer delays, for reasons that will be discussed later.

It appears that the emergence of all the visible G, D and RBM bands occurs at roughly the same time. From Figure 13, all three band types also seem to grow at roughly the same rate, before cessation of growth and saturation in Raman signal intensity. The growth rate in all visible bands seems to be highest within the first 40 seconds (8 frames) after appearing. By t=250s, all these visible bands appear to have stopped (or almost stopped) growing. These growth trends warrant further analysis and will later be discussed at length.

As is typical among all Co samples, the G band is by far the most intense of all the analyzed Raman bands. The G+ peak (at 1577 cm^{-1}) is dominant, although a slight asymmetry reveals barely resolved G- character (at ~1515 cm^{-1}). The D band (at ~1327 cm^{-1}), though clearly seen to emerge, maintains a significantly lower intensity, indicating overall low defect generation. On all the Co samples, these low intensity D bands are typical and the resulting extracted low signal/noise Raman D band area makes it difficult to calculate meaningful kinetic I_D/I_G ratios. Additionally, because the G and D band intensities may themselves be temperature dependent, the direct quantitative comparison of I_D/I_G ratios at different temperatures may be misleading.

Finally, in Figure 13, the only visible RBM peak whose signal is strong enough to extract is the one at ~277 cm^{-1}. This is actually the second of two high intensity RBM peaks we have mentioned, which we shall henceforth refer to as RBM-2. Generally speaking, the RBM-2 peak was found to be present over a wide range of temperatures,

but tended to be of higher intensity at growth temperatures of 813°C and lower. Unfortunately, as seen in the Figure, RBM-2 emerges atop substrate related background features located from 150-400 cm^{-1}, and this can complicate subsequent RBM analysis, as can its proximity to neighboring RBM peaks.

To better understand the final growth results on this 725°C grown sample, we to contrast the pre- and post- growth spectra, as presented in Figure 14.

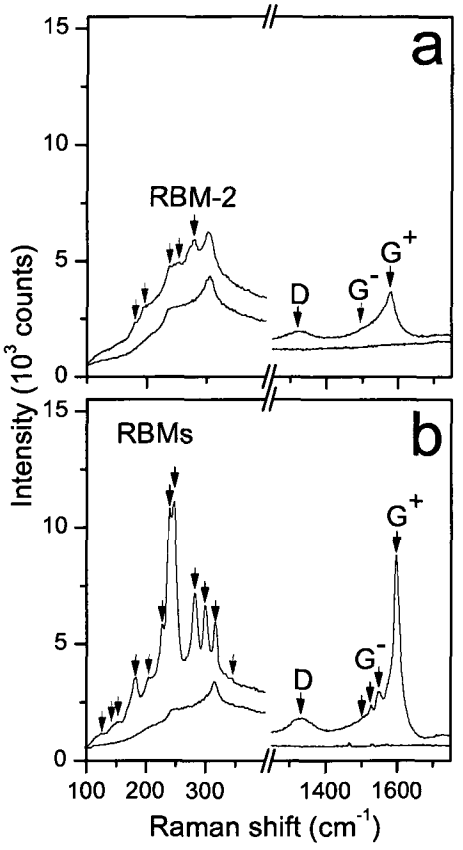

Figure 14: Pre-growth (black) and post-growth (red) Raman spectra for the Co sample grown at 725°C taken at: (a) 725°C and (b) room temperature. Each frame was exposed for 15 seconds. Black arrows indicate high intensity, well separated Raman bands. Gray arrows indicate low intensity and/or poor resolved bands. Adapted from ref. [57].

First notice that the high temperature background in (a) is higher and more sloped than in (b). The post-growth (in red) G, D and RBM peaks at low temperatures are generally higher, sharper and more feature-rich than their corresponding broadened high temperature peaks. Numerous room temperature G- peaks (at 1503 cm^{-1}, 1529 cm^{-1} and 1549 cm^{-1}) are not visible at 725°C. As described in Appendix C, the room temperature D and G^- peaks (at 1331 cm^{-1} and 1597 cm^{-1}, respectively) are slightly downshifted at the growth temperature (to 1325 cm^{-1} and 1577 cm^{-1}, respectively). The intense, room temperature G+ peak is clearly visible at 1598 cm^{-1} and after extracting the total G and D Raman areas under the spectral data extraction/correction method outlined in Appendix B, the room temperature I_D/I_G ratio is calculated to be ~0.13. This relatively low value, combined with the appearance of numerous room temperature RBMs indicates that the SWNTs that are present in the sample are of very good crystallinity. Due to the change in resonance conditions between high and low temperatures and peak shifting (see Appendix C), the high temperature RBM peaks we are interested in are not clearly visible at room temperature.

The SWNT diameters associated with the visible, room temperature RBMs can be roughly estimated by substituting a=248 $nm \cdot cm^{-1}$ and b=0 into Equation 6, previous used for isolated CNTs on silicon. [19,66] Thus, RBM peaks at 182 cm^{-1}, 206 cm^{-1}, 227 cm^{-1}, 240 cm^{-1}, 246 cm^{-1}, 281 cm^{-1}, 299 cm^{-1} and 317 cm^{-1} roughly correspond respectively to diameters of 1.36 nm, 1.20 nm, 1.09 nm, 1.03 nm, 1.00 nm, 0.88 nm, 0.83 nm, 0.78 nm. The applied a and b values are less accurate for determining the diameter of SWNTs with $d_t < 1$nm, due to curvature and chirality effects. [16,19,66]

The G, D and RBM-2 kinetic areas from Figure 13 are intense enough to track with time, using the method in Appendix B. Because all three signals eventually saturate in intensity with time, the kinetic areas can also be scaled by these respective maximum values. The un-scaled and scaled evolution curves are presented in Figure 15.

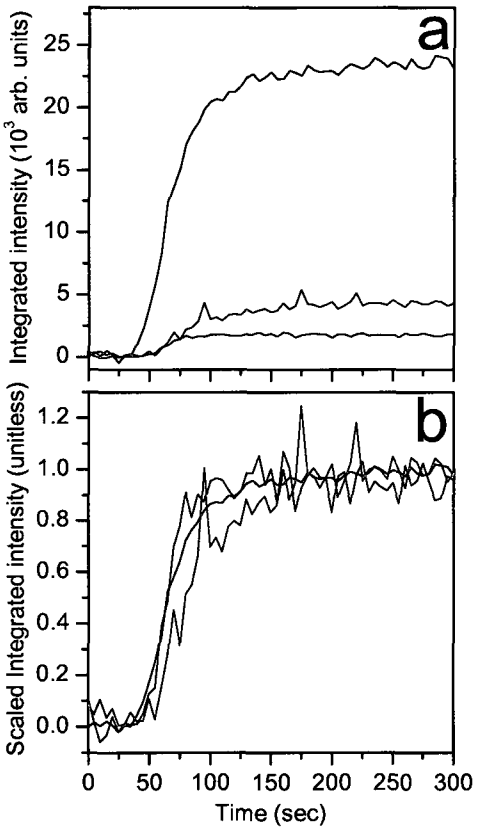

Figure 15: Time evolution of the background corrected integrated G band (black), D band (green) and RBM-2 band (blue) intensities for the Co sample grown at 725°C: (a) un-scaled and (b) scaled to the final saturated intensities. Data is sampled continuously with a 5 second integration time. Adapted from ref. [57].

Despite their differences in intensities, the three corrected Raman areas grow at similar rates, with both the un-scaled and scaled evolution curves sharing the same overall shape. For all curves, the initial growth spurt at 30 seconds appears to occur exponentially, followed by an immediate slow-down to a roughly linear growth rate and

eventual exponential slow-down and termination from 75 seconds onwards. The 5 second kinetic exposure time used for all the Co samples is used to achieve a better signal/noise ratio for all Raman bands, but only the intense G band (black) results in a relatively smooth scaled plot. Regardless, all three scaled bands in Figure 15(b) appear to track each other to within experimental uncertainty, although the D band may lag slightly behind the G and RBM-2 band.

The G and RBM-2 bands closely track each other, indicating that the growth rate of the SWNT (or thin walled MWNT) corresponding to RBM-2 consistently scales to the growth rate of the sp^2 dependent G band. Similar G/RBM-2 tracking was observed on other low temperature Co samples. Note that if SWNTs that are present do not contribute to the RBM, they can still contribute to the G band intensity because the G band and RBM have different resonant windows. The tracking therefore provides indirect evidence that the average growth rate of all growing SWNTs, matches that of a single SWNT species, namely RBM-2. In other words, in addition to the RBM peaks, the G band evolution may also be a reliable indicator of SWNT growth, under our growth conditions.

In order to highlight important temperature related trends, these low temperature results were compared with those obtained from a typical high temperature sample. As an example, Figure 16 shows the kinetic spectra of a Co sample grown at 875°C. As with Figure 13, the time sequence progresses from bottom to top with each frame exposed for 5 seconds, although frames are only shown every 25 seconds in Figure 16.

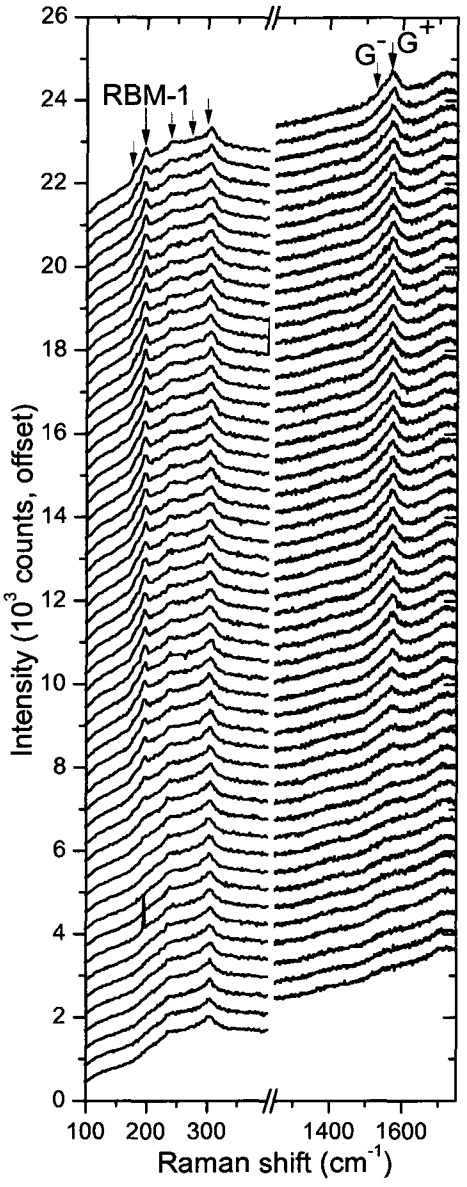

Figure 16: Kinetic Raman spectra from the Co sample grown at 875°C. The spectra from t=0s (bottom frame) to t=825s (top frame) is presented in intervals of 25 seconds, with an individual frame exposure of 5 seconds. Black arrows indicate high intensity, well separated Raman bands. Gray arrows indicate low intensity and/or poor resolved bands. Adapted from ref. [57].

There are several key differences between Figures 13 and Figure 16, the first being the absence of any clearly visible D and RBM-2 bands in Figure 16. The D band absence is understood; assuming that all other experimental parameters are held constant,

it is well established that D band intensities are lower at increasing CVD growth temperatures. There is thus an overall, observable decrease in D band intensity among the Co samples with increasing growth temperatures, with the D band intensity becoming too low to analyze in growth runs performed above 788°C. The RBM-2 band could not be easily observed above temperatures 813°C, although the variation in band intensity below this temperature is far less controlled than it is for the D band. It is possible that an extremely weak RBM-2 contributes to the spectra in Figure 16, but it cannot be distinctly identified over the substrate background.

At high temperatures, the most intense RBM peak corresponds to RBM-1 (located at ~197 cm^{-1}). Assuming that the near inverse relationship between SWNT diameter and RBM peak location holds true at elevated growth temperatures, RBM-1 corresponds to a SWNT species with a diameter roughly 1.5 times larger than that of RBM-2. The fact that RBM-1 is most intense at high temperatures and RBM-2 is most intense at low temperatures is consistent with earlier work showing that higher diameter CNTs will usually grow under higher growth temperatures, using similar catalyst formulations and CVD conditions. [57,67,68] However, Yao *et al.* was able to grow thinner SWNTs at higher temperature and describes how growth temperature can be used to tune SWNT distributions, to a certain extent. [69] For the purposes of data extraction, RBM-1 was only intense enough to analyze on Co samples grown above 775°C. As seen in Figure 16, RBM-1 is often accompanied by a neighboring RBM peak that forms a spectral shoulder at 179 cm^{-1} that is too difficult to extract due to its spectral location and low intensity. Across all our grown Co samples, either RBM-1 or RBM-2 is present and evolves with sufficient intensity to analyze.

Another important difference concerns the delay in both peak emergence and subsequent growth. The kinetic data reveals an initially very low G band, eventually exhibiting an asymmetric G^- shoulder, emerges at the same time as RBM-1, 220 seconds after opening the bubbler. To indicate this start time, the 225 second frame in Figure 16 is shown in green, although the two bands may not be apparent until the next 2-3 frames (50-75 seconds), as indicated in blue. Additionally, the growth of the bands only appear to significantly slow down 10-12 frames (250-300 seconds) after the onset, which is significantly slower than the roughly 50 seconds before saturation in Figure 13. These observations are typical of a more general phenomenon observed over all the Co samples, namely that as the growth temperature is increased, the time required for the detected G and RBMs bands to simultaneously appear is increased, while the subsequent Raman band growth rates also slow down. The phenomena shall be further discussed in Section 6.5.

Figure 17 shows the pre- and post-growth spectra of the 875°C grown sample, analogously to Figure 14, at both the growth temperature and room temperature. As mentioned, the high temperature spectral background in Figure 17(a) is substantially higher than the one in Figure 14 due to the increased blackbody. Above 875°C the blackbody makes it very difficult to identify the G band baseline and complicates RBM extraction. Also, the room temperature D band (still at 1331 cm^{-1}) is significantly lower than in the 725°C sample, again confirming the high crystallinity on the sample; the room temperature I_D/I_G ratio is ~0.02. Numerous room temperature RBMs again become visible after cooling the sample, although the spectral weight distribution differs from

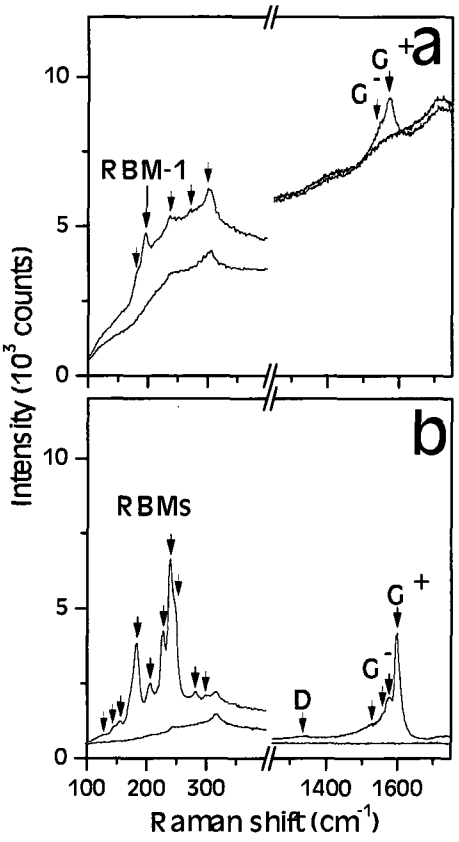

Figure 17: Pre-growth (black) and post-growth (red) Raman spectra for the Co sample grown at 875°C taken at: (a) 875°C and (b) room temperature. Each frame was exposed for 15 seconds. Black arrows indicate high intensity, well separated Raman bands. Gray arrows indicate low intensity and/or poor resolved bands. Adapted from ref. [57].

that of Figure 14, with more weight being placed on high diameter (lower wavenumber) SWNTs.

Again substituting a=248 nm·cm^{-1} and b=0 into Equation 6, this time for RBM peaks at 155 cm^{-1}, 184 cm^{-1}, 206 cm^{-1}, 227 cm^{-1}, 240 cm^{-1}, 246 cm^{-1} and 281 cm^{-1}, yields respective SWNT diameters of roughly 1.60 nm, 1.35 nm, 1.20 nm, 1.09 nm, 1.03 nm, 1.01 nm, 0.88 nm.

Many of these same peaks, such as the high intensity peaks near ~240 cm^{-1}, do reappear from Figure 14 however, but it is still unclear whether any of the visible peaks

are related to the high temperature RBM-1 and RBM-2. The final room temperature G+ peak location at 1598 cm^{-1}, unchanged from Figure 14, and several G- peaks (e.g. at 1526 cm^{-1} and 1577 cm^{-1}) again appear at room temperature. As a general rule, across all the Co samples, there is typically little shift in the room temperature positions of the D, RBM and G peaks, although the intensity distribution of RBMs and G- peaks can vary greatly.

The growth evolution of the RBM-1 and G band areas can also be compared in a manner analogous to Figure 15, as depicted in Figure 18. Again, both the un-scaled and scaled plots are shown.

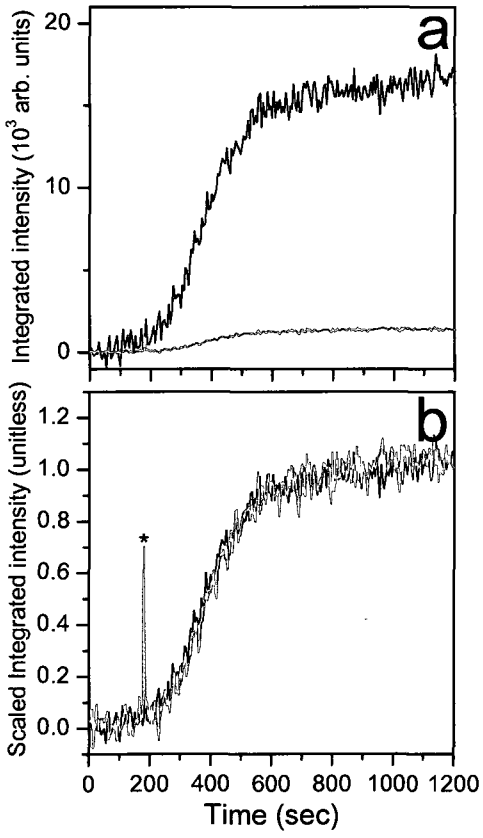

Figure 18: Time evolution of the background corrected integrated G band (black) and RBM-1 band (orange) intensities for the Co sample grown at 875°C: (a) un-scaled and (b) scaled to the final saturated intensities. The asterisk denotes a spike in intensity due to a cosmic ray event. Data is sampled continuously with a 5 second integration time. Adapted from ref. [57].

The same characteristic evolution form displayed by all three bands in Figure 15, are again present for both the G and RBM-1 band in Figure 18. However, as noted, the detectable band-growth onset and the time scale for the growth have been delayed. In fact, growth still has not fully saturated even after 1200 seconds. Thus, because the curve is well sampled, we can clearly see change in growth rates from exponential increasing, to linearly increasing, to exponential decreasing. The scaled plots in Figure 18(b) again show very close tracking between the G band and an RBM band and is typical of all high growth temperature samples. This suggests that G-RBM tracking occurs independently of which SWNT species grow on each sample.

In one or two cases, at intermediate temperatures, both RBM-1 and RBM-2 produce signals are just intense enough to analyze concurrently with the G band. The best example of this is the Co sample grown at 813°C, whose kinetic spectral frames are presented in Figure 19, in the same manner as Figures 13 and 16. This time, however, frames are only shown every 20 seconds.

The detectable band-growth onset and the time scale for the 813°C grown sample are delayed compared to that of the 725°C sample (Figure 13), but prolonged compared to the 875°C sample (Figure 16). Also, as expected, the spectral background is higher than that of the 725°C sample, but lower than that of the 875°C. The D band is again absent. The earliest detectable G and RBM-1 band onsets occur at 40 seconds (in green), although in Figure 19 the onset is more apparent roughly 20 seconds later (in blue). Because RBM-2 still isn't as intense as desired, it is difficult to resolve exactly when it

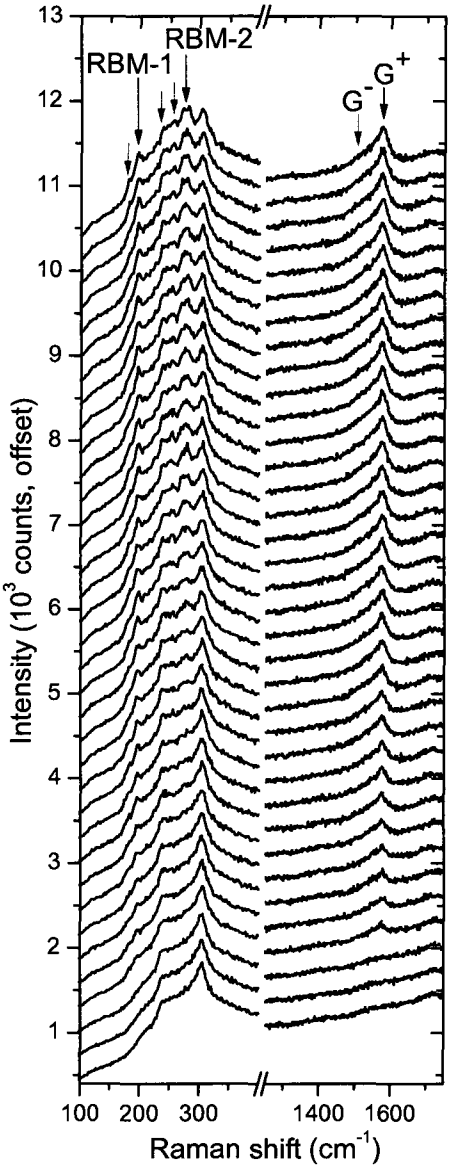

Figure 19: Kinetic Raman spectra from the Co sample grown at 813°C. The spectra from t=0s (bottom frame) to t=700 (top frame) is presented in intervals of 20 seconds, with an individual frame exposure of 5 seconds. Black arrows indicate high intensity, well separated Raman bands. Gray arrows indicate low intensity and/or poor resolved bands. From ref. [65].

first emerges above the substrate related background peaks (i.e. 240 cm^{-1} and 306 cm^{-1}). In other words, because growth occurs over a relatively prolonged time frame, the initially weak and obscured RBM-2 band is difficult discern over the signal/noise

threshold, until it achieves a minimum amount of intensity. RBM-2 has emerged sometime before the 140 second frame (in violet), concurrently with a weaker neighboring peak at ~255 cm^{-1}, which is too weak to accurately track entirely. Other RBMs are also too weak to track, although their presence about RBM-2 also adds to the difficult of extracting the kinetic RBM-2 area.

In Figure 20, the temperature dependant pre- and post-growth plots for the 813°C sample are again presented in the same manner as Figures 14 and 17.

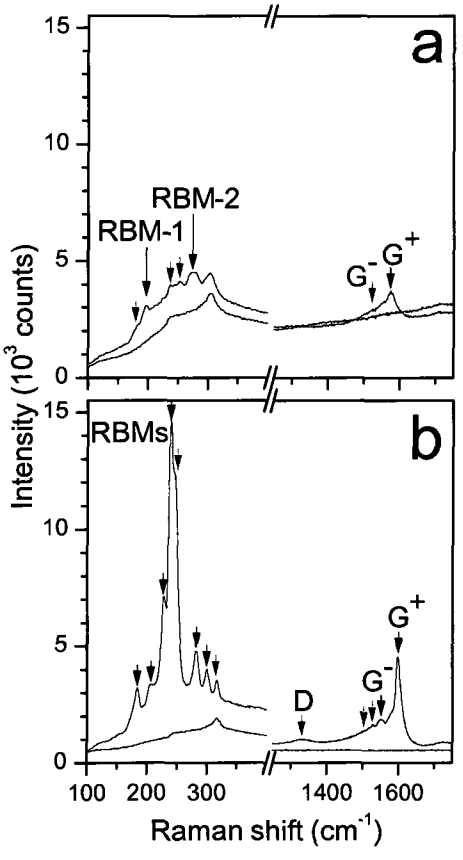

Figure 20: Pre-growth (black) and post-growth (red) Raman spectra for the Co sample grown at 813°C taken at: (a) 813°C and (b) room temperature. Each frame was exposed for 15 seconds. Black arrows indicate high intensity, well separated Raman bands. Gray arrows indicate low intensity and/or poor resolved bands. From ref. [65].

Individually, the final RBM-1 and RBM-2 bands are not as intense as those in Figures 17 and 14, respectively, but they are sufficiently intense for analysis. At room temperature, G+ (at 1598 cm^{-1}), G- (e.g. at 1551 cm^{-1}, 1528 cm^{-1} and 1505 cm^{-1}) and D (1329 cm^{-1}) bands are again clearly resolved and the I_D/I_G ratio is ~0.04, which is lower than that of the 725°C sample. As usual, many room temperature RBMs are present. The low and high diameter SWNT-RBMs (respectively around 250-300 cm^{-1} and 150-200 cm^{-1}) are at intermediate intensities, as expected. [16]

The Equation 6 diameter calculation (again with a=248 $nm \cdot cm^{-1}$ and b=0), for RBM peaks at 184 cm^{-1}, 207 cm^{-1}, 228 cm^{-1}, 240 cm^{-1}, 247 cm^{-1}, 283 cm^{-1} and 301 cm^{-1}, respectively yield diameters of roughly 1.35 nm, 1.20 nm, 1.09 nm, 1.03 nm, 1.00 nm, 0.88 nm, 0.82 nm.

The G, RBM-1 and RBM-2 evolution curves are presented in Figure 21, in the manner of Figures 15 and 18. The unscaled integrated G band intensity is far higher than for either of the analyzed RBMs. The initial exponential increase in the G and RBM-1 intensities is more abrupt than in Figures 15 and 18, but otherwise the growth evolution curves share the expected shape. As with Figure 18, the scaled G and RBM-1 bands track each other very clearly, but it remains unclear whether the start time for the detectable RBM-2 band has been delayed or not. As mentioned the RBM-2 data is difficult to extract and meaningful intensity data cannot be obtained prior to ~150 seconds. Thus, in order to properly scale RBM-2 we set its scaled value at 175 seconds to equal 0.45, which is the matching value of the scaled G band intensity. After this time, all three bands are found to closely track. This provides evidence, at least past a minimum amount of RBM-2 growth, that there is little change in the diameter distribution of the RBM over time; i.e.

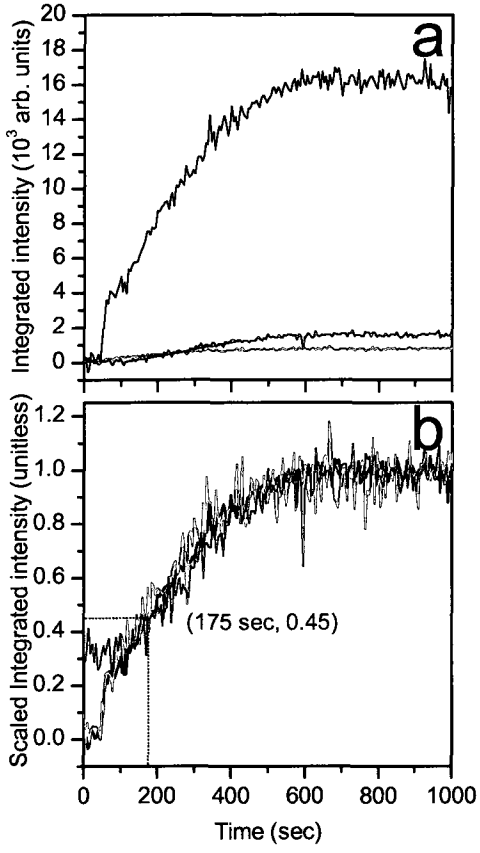

Figure 21: Time evolution of the background corrected integrated G band (black), RBM-1 band (orange) and RBM-2 (blue) intensities for the Co sample grown at 813°C: (a) un-scaled and (b) scaled to the final saturated intensities. Data is sampled continuously with a 5 second integration time. RBM-2 values from t=0-150s cannot be properly background corrected and are inaccurate. The scaled RBM-2 intensity at 175 seconds is therefore set to 0.45 to match the G band value. From ref. [65].

that different diameter SWNTs can grow at the same rate.

For completeness, the un-scaled G, D, RBM-1 and RBM-2 intensity evolution curves for all 14 Co samples in Appendix D. These Raman bands were calculated whenever they were sufficiently intense, although under our current CVD method the final Raman band intensity of individual peaks could not be well controlled, outside of the overall temperature dependent trends we have described. In Appendix E we have also

shown the final, tabulated room temperature I_D/I_G ratios of all 14 Co samples. The overall decrease of this ratio with increasing temperatures is explicitly shown.

6.2 Co sample SEM images

Overall, Co samples produced primarily short surface CNTs at varying diameters and yield. The upper detector of a Hitachi S-4700 was used to take SEM images from the Co samples presented in Section 5.1 after CVD growth to characterize CNT yield.

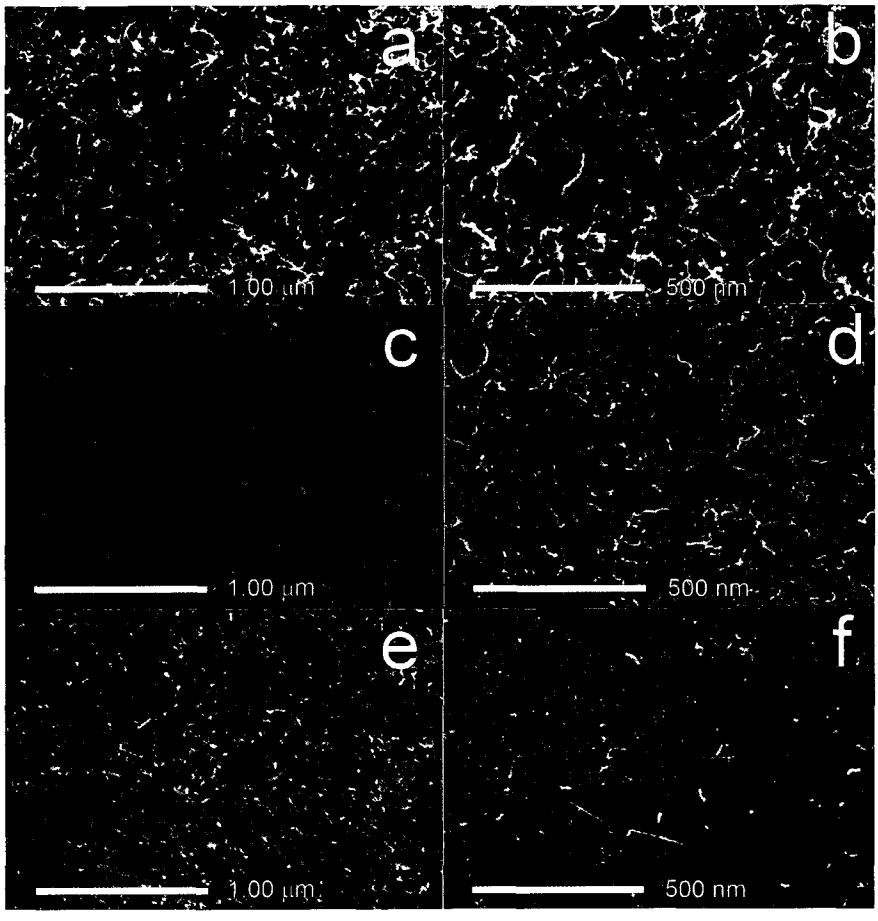

Figure 22: SEM images of the Co sample grown at: (a) 725°C, with 1 kV accelerating voltage, (b) 725°C at 5 kV (c) 813°C at 1 kV (d) 813°C at 5 kV., (e) 875°C at 1 kV and (f) 875°C at 5 kV. Images (b), (e), and (f) are used from ref. [57].

Typical images from the 725°C, 813°C, and 875°C samples are shown in Figure 22, in order of increase growth temperature, taken at both 1 kV and at 5 kV accelerating voltage.

The 725°C grown sample imaged at 1 kV in Fig. 22(a) shows relatively short and unaligned surface CNTs that are abundant, clearly visible, and undergoing charging. CNT thicknesses vary; several SWNTs may be present, alongside possible bundled SWNTs or MWNTs. Fig. 22(b), taken both at a higher magnification and at 5kV, reveals the presence of nanoparticles, less than 10 nm in diameter, interspaced at roughly the same distance. These nanoparticles likely originate from the catalyst and appear to be roughly the same size or smaller than the diameters of the visible CNTs.

The 813°C grown sample imaged at 1 kV and 5 kV a.v. (Figs. 22(c) and (d), respectively) shows far fewer long or thick CNTs than the ones in Figs. 22(a) and (b). Only short, tangled surface CNTs are seen. Comparing Figs. 22(b) and (d) shows little change visible in nanoparticle size and density.

Growth on the 875°C sample imaged at 1 kV (i.e. Fig. 22(e)) appears sparser than in the lower temperature samples and fewer long CNTs are present. This is consistent with the lower overall G and RBM Raman intensities obtained in the 875°C sample compared those of the 725°C and 813°C samples. It is nearly impossible to determine actual CNT diameters from the 875°C sample via SEM. However, as with the 813°C grown sample, fewer very large diameter CNTs appear to be present, perhaps due to the decreased numbers of MWNTs expected in high temperature growth. Fig. 22(f) reveals catalytic nanoparticles that appear to be roughly the same size, but perhaps slightly more densely packed than in Figs. 22(b) and (d). This may suggest that the decrease in growth

rates with increasing temperature is unrelated to changes in nanoparticle size. The few CNTs visible under 5kV also appear to be straighter than for these lower temperatures growths.

6.3 Co-alumina sample spectral evolution

In order to investigate the effect of catalyst dependence on the temperature growth trends we have observed, 10 Co-alumina samples were grown between 675°C – 825°C. These samples are discussed in ref. [65]. At growth temperatures of 850°C and above, no CNTs were formed.

The CNT nucleation behaviour on the Co-alumina samples could be more thoroughly examined than the Co samples. As mentioned, while Co samples resulted in the growth of relatively high quality, surface CNTs in low yields, the Co-alumina samples produced relatively low quality, high yield CNT forests. This overall high yield results in, among other things, a significantly stronger G band intensity, which allows us to use shorter kinetic integration times of 0.7 seconds instead of 5 seconds. In other words, we obtain high signal/noise spectral data even at low sampling rates.

However, there are also major disadvantages to using the Co-alumina samples for Raman studies. Apart from the higher numbers of defective CNTs, high intensity kinetic RBM data is either absent or at too low an intensity to be useable, perhaps due to the low numbers of grown SWNTs versus MWNTs. Additionally, over time, especially at lower temperatures, the resulting CNT forests frequently grew so high that past a certain forest height, the incident light was unable to fully penetrate the top CNT layers. Because the optical apparatus is focused on the sample surface and was not refocused during growth,

there is gradual loss in the scattered Raman surface signal (indicated by the disappearance of the Si peak) and a large rise in the spectral background below the G and D bands. Accurate background correction therefore eventually becomes impossible. Thus, to ensure that we only analyze the evolution of the CNT growth front, we focus our analysis on the initial CNT growth evolution. Otherwise, we proceed with the Co-alumina sample analysis by the same manner we analyzed the Co samples.

A typical low temperature, spectral kinetic series for the 700°C grown Co-alumina sample is presented in Figure 23. Each frame is exposed for 0.7seconds, with a frame displayed every 4.9 seconds from bottom to top. As usual, the time spectra are arranged from bottom to top, from t=0s (bubbler opening) to t=126.7s.

As with the low temperature Co samples, both the G and D bands (at ~1571 cm^{-1} and ~1324 cm^{-1}, respectively) first become detectable at roughly the same time. However, instead of the 30 second onset observed for low temperature Co samples, the bands emerge at the delayed time of 60 seconds instead (green frame). Note the relatively large D band compared to the Co sample data. Growth of the two bands appears to occur concurrently and, in this sample, we are able to record the stage when the band intensities start to saturate at roughly 125 seconds (roughly 2-3 frames from the top). After this time, as noted above, the G and D band intensities actually start to *decrease* due to the out-of-focus and opaque samples imaging conditions caused by excessive forest height, eventually becoming submerged by the rising background and becoming undetectable. In this sample, no RBMs were detected at the growth temperature.

The pre- and post-growth Co-alumina spectra for the samples grown at 700°C differ substantially from those of the Co spectra. These spectra, both at room and growth temperatures, are presented in Figure 24. The Si band is displayed to illustrate its drop in

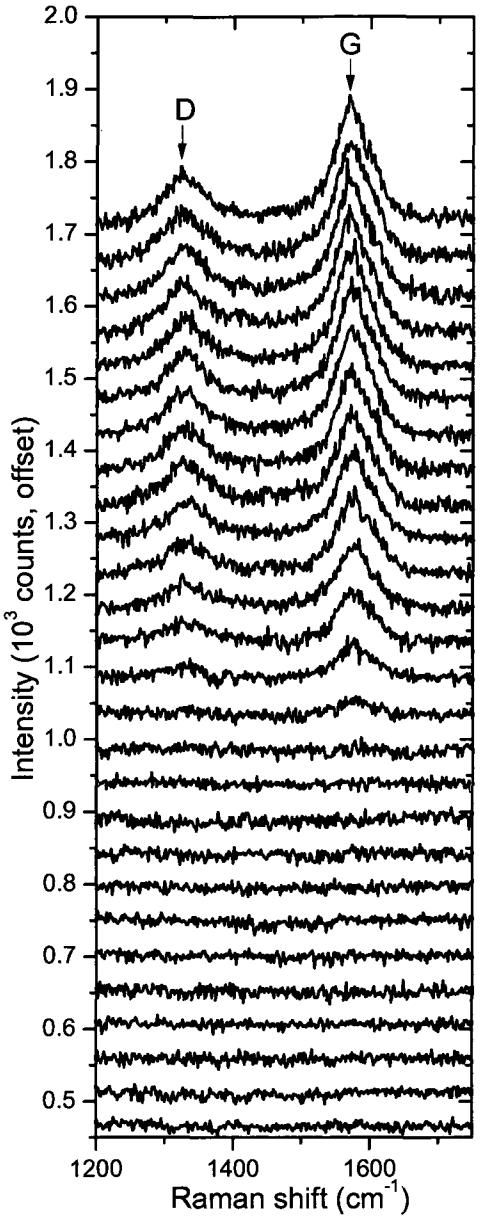

Figure 23: Kinetic Raman spectra from the Co-alumina sample grown at 700°C. The spectra from t=0s (bottom frame) to t=126.7s (top frame) is presented in intervals of 4.9 seconds, with an individual frame exposure of 0.7 seconds. Black arrows indicate high intensity, well separated Raman bands. From ref. [65].

intensity during growth. By comparison, the Si band intensity remains fairly constant for the Co samples.

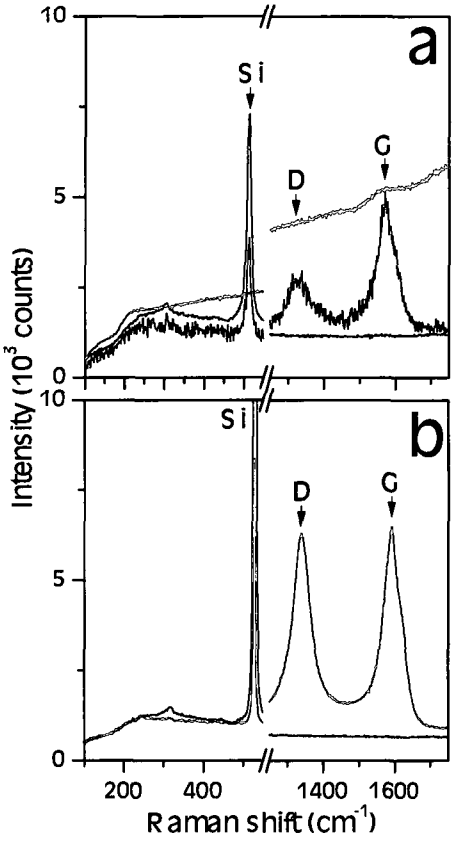

Figure 24: Pre-growth (black), intermediate growth (blue) and post-growth (red) Raman spectra for the Co-alumina sample grown at 700°C taken at: (a) 700°C and (b) room temperature. The pre-growth and post- growth spectra used exposure times of 15 seconds. The intermediate frame, taken 100 seconds after opening the bubbler, was exposed for 0.7 seconds and scaled by a factor of 15/0.7. Black arrows indicate high intensity, well separated Raman bands.

To highlight the substantial rise in background starting at around to t=125s, a spectrum taken at an intermediate time (t=100s) is included. Initially, at both room temperature and 700°C, the pre-growth spectra are not noticeably different from those of the Co samples. However, as seen in the t=100s spectrum, even after only t=100s, the CNT forest has grown so tall and thick that the intensity of the first order Si band (at

~514 cm^{-1}) has already fallen substantially. At this point the spectral background below the D and G band remains relatively flat, but this background begins to rise significantly shortly (i.e. ~25s) afterwards. The high temperature post-growth spectral background has almost completely obscured the G and D signal and also further obscured the SiO_2 background, where RBMs would be typically present. However, no resonant RBMs are present for this sample, as is typical for all low temperature Co-alumina samples, which possibly have a higher MWNT yield.

Post-growth spectra for this sample were not stable, and exposure to the laser caused drops in observable Raman bands. The shown post-growth spectrum may be from a partially burnt or annealed region on the forest. Although the G and D bands (at ~1592 cm^{-1} and ~1340 cm^{-1}, respectively) are clearly visible in this region, on portions of the forest where the Raman spectra remained stable, the G and D bands still appear obscured. In this case, the corresponding I_D/I_G ratio was found to be ~0.96, a fairly high value, although this likely does not accurately reflect CNT purity close to the sample surface. On other grown Co-alumina samples that where purged continuously, the Raman spectra remained stable. Finally, the G band appears more symmetrical than for the Co samples. The lack of any asymmetric G- might indicate low SWNT content.

As with the low temperature Co samples, the G and D band evolution curves of the 700°C grown Co-alumina sample appear to track each other, as depicted in Figure 25 (in black and green, respectively). The kinetic Raman area of first order Si band (violet) is also displayed to highlight its variation; in Figure 25(b), it has been scaled to its maximum intensity.

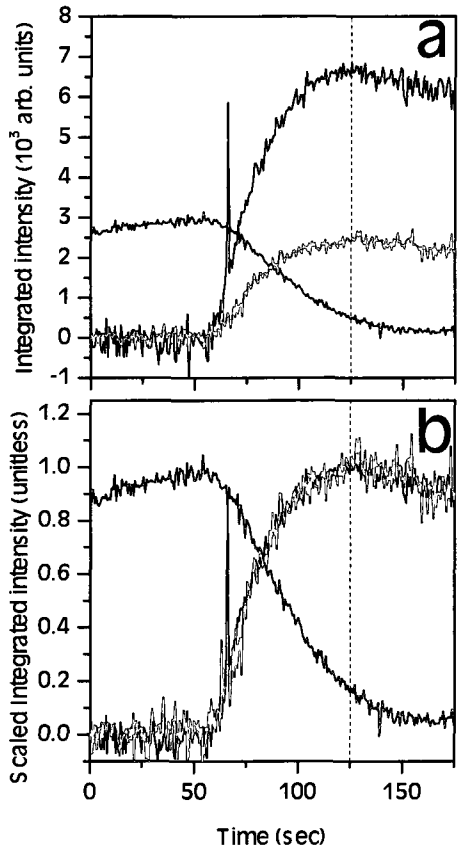

Figure 25: Time evolution of the background corrected integrated G band (black), D band (green) and first order Si band (violet) intensities for the Co-alumina sample grown at 700°C: (a) un-scaled and (b) scaled to the final saturated intensities. Data is sampled continuously with a 0.7 second integration time. Data extracted after t=125s (dotted line) cannot be accurately background corrected. Adapted from ref. [65].

As indicated by the dotted line, by t=125s the Si band intensity has already fallen significantly, before dropping to 0 at roughly t=160s (not shown). This intensity drop is due to light being unable to penetrate the opaque CNT layer due to excessive forest thickness and not due to any physical/chemical change to the Si substrate. This drop, along with the large rise in the spectral background below the G and D bands, indicate that G and D integrated intensities are only meaningful before t=125s. However, the close D/G tracking is sufficient to show that there is little change in I_D/I_G ratios, and thus CNT crystallinity, at early growth times.

The D/G tracking is consistent for all Co-alumina samples below 725°C, but as with the Co samples, the D band intensity is found to drop significantly with growth temperature, such that it is essentially undetectable during growth at 800°C. Due to its weak signal above 725°C, it is unclear whether the first appearance of the D band signal lags behind the G band or whether this appearance occurs below the signal/noise level and cannot be directly observed. Regardless, since close tracking is observed between the sp^2 related G band and the sp^3 related D band, one can conclude that, at least over a significant range of temperatures, sp^2 and sp^3 hybridized carbon molecules are deposited on the sample surface at the same rate. Interestingly, the *in situ* Raman study by Dittmer *et al.* of CVD grown CNTs showed a strongly evolving I_D/I_G ratio evolution during growth. [7] It is possible that CNT crystallinity is sensitive to differences in growth method and the carbon source gas (in this case, ethylene versus ethanol). It should be noted that Dittmer *et al.* paused growth and cooled the sample to measure the Raman spectra, and the I_D/I_G ratio evolution may have been affected by this. [7] Also, Picher *et al.* observed a I_D/I_G ratio that gradually increased with time at very high temperatures, attributed to amorphous carbon formation. [8] It is possible that we did not reach high enough growth temperatures to observe this phenomenon.

The pre- and post-growth spectra from a Co-alumina sample grown at 775°C are shown in Figure 26. After t=150s, the background rises and G and D cannot be extracted meaningfully. Similarly to the Co samples, the I_D/I_G ratios of the Co-alumina samples decrease with increasing growth temperature. The spectral evolution of all the Co-alumina samples appears very similar to the 700°C case, with two notable differences.

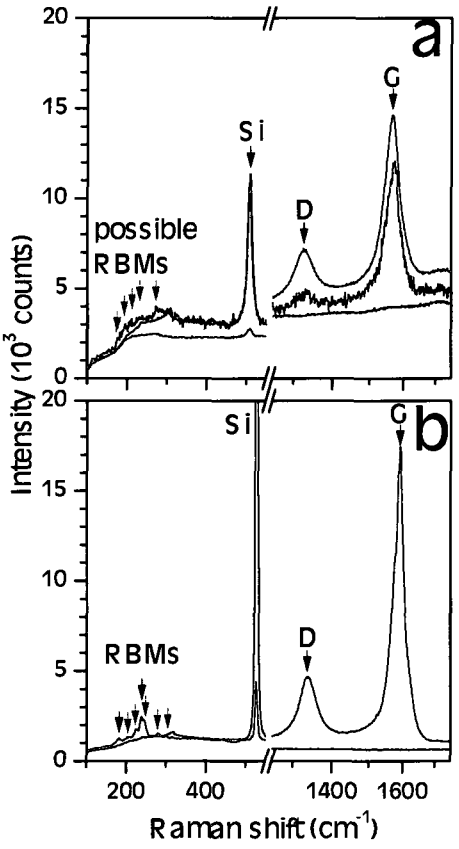

Figure 26: Pre-growth (black), intermediate growth (blue) and post-growth (red) Raman spectra for the Co-alumina sample grown at 775°C taken at: (a) 775°C and (b) room temperature. The pre-growth and post-growth spectra were exposed for 15 seconds. The intermediate frame, taken 150 seconds after opening the bubbler, was exposed for 0.7 seconds and scaled by a factor of 15/0.7. Black arrows indicate high intensity, well separated Raman bands. Gray arrows indicate low intensity and/or poor resolved bands. Adapted from ref. [65].

One difference is that, after cooling to room temperature, RBMs were detectable on post-growth Co-alumina samples grown at 775°C and higher temperatures. However, as seen on Figure 26, these RBMs (between ~175-300 cm^{-1}) are of much lower intensity that those obtainable from the Co samples. More importantly, although partially visible, the associated high temperature RBM bands were still too weak to extract, especially given the added complications of background correction. Thus, the RBM scaling and SWNT diameter evolution dynamics on the Co-alumina could not be studied.

Another difference is that, again similarly to the Co samples, as temperature is increased, the first appearance of the G band is delayed and the overall rates of CNT growth are slowed down. One side effect of this is the intermediate-frame in Figure 26; due to slow down in growth rates, the spectral background only begins to change at 150 seconds, instead of 100 seconds, as it did in Figure 24. Above 800°C, due to the diminished forest height after 5 minutes, the spectral background below the G band remains flat for the duration of the run, although the G band signals remains relatively intense throughout. We investigate the meaning behind this change in rate kinetics in the following section.

For complete reference, as with the Co samples, the un-scaled G and D intensity evolution curves for all 10 Co-alumina samples are presented in Appendix D, wherein the slow down in band emergence and overall growth rates is apparent. As before, only sufficiently intense Raman bands were analyzed. The final, tabulated $I_D I/_G$ band ratios for the Co-alumina samples are also shown in Appendix E.

6.4 Co-alumina sample SEM images

Co-alumina samples were examined by SEM. Both visually and under SEM, the CNT film appears qualitatively thinner at progressively higher temperatures. Typical SEM images from the 700°C and 775°C grown samples are shown in Figure 27(a) and (b), respectively. Because vertical CNT forests are present on all Co-alumina samples, the images have been taken with a vertical axial tilt of 25° to show forest depth. Fig. 27(a) shows a small kink near the forest surface.

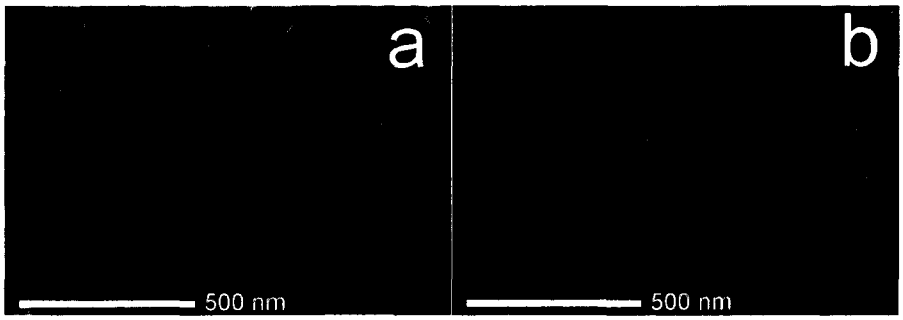

Figure 27: SEM images taken using a 1 kV acceleration voltage at a 25° tilt with the vertical axis; Co-alumina samples grown at (a) 700°C and (b) 775°C.

The micrographs appear significantly different than those of the Co samples. Imaged CNT forests show some degree of vertical alignment. Catalytic nanoparticles were not observed near the tops of the imaged forests. Macroscopically, the 700°C sample appeared to be coated with a black film, while the 775°C sample film was thinner and more translucent. No such coatings were visible on the Co samples. Thinner CNTs that are visible on the 775°C grown sample, do not appear present on the 700°C grown sample, perhaps indicating a difference in MWNT content or the degree of CNT bundling.

6.5 Proposed four step growth evolution process and characteristic energy analysis

The growth evolution curves for all analyzed G, D, RBM-1 and RBM-2 bands for both the Co and Co-alumina samples, share the same characteristic shape, depicted schematically in Figure 28.

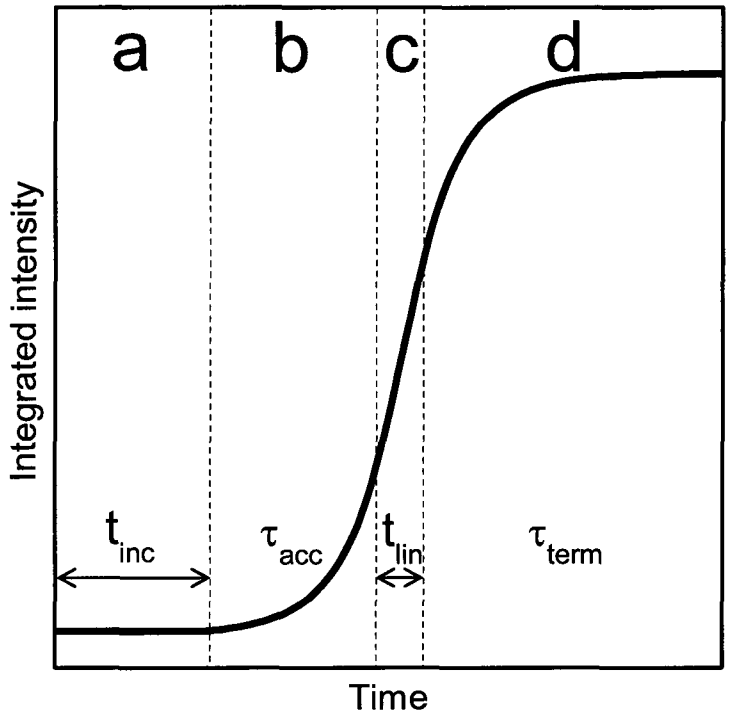

Figure 28: Proposed 4-step growth process for all G, D and RBM integrated intensities: (a) incubation in the presence of ethanol; (b) onset and accelerating growth; (c) linear growth; (d) growth termination/saturation. The time constants from steps (b) and (d) are obtained from exponential fits, while those from steps (a) and (c) are the measured step durations. Adapted from ref. [65].

In this schematic, we have divided the Raman intensity growth process into four separate steps: incubation, acceleration, linear growth and termination. We propose that the change in characteristic growth rates during each step relates to a specific change in the growth process of the CNTs.

Initially in each growth run, when the bubbler is opened, we observe a delay period before the onset of any detectable Raman band. This delay has two components. The first component is the transient travel time required for the ethanol to reach the sample surface. It is assumed that this time is roughly 30 seconds, corresponding to the shortest delay time seen across all the analyzed samples, namely the low temperature Co samples. However, on both sample types, the total delay time was found to increase with increasing temperatures. Because the travel time is fixed due to its reactor dependence, we attribute the second component of the delay to a so-called incubation step, depicted in Figure 28(a).

For each analyzed Raman band, the incubation time (i.e. t_{inc}) was directly measured as the time difference between the first 30 seconds of the run and the first spectral appearance of the band above the signal-to-noise threshold. Because this stage precedes detectable Raman band growth, this growth stage likely corresponds to the initial collection of the carbon molecules on to the catalytic nanoparticles just prior to CNT formation. It is therefore unsurprising that, at a given growth temperature, the incubation time was found to be dependent on the catalyst formulation, with t_{inc} for the Co-alumina samples being longer than that of the Co samples. For example, at 800 °C the t_{inc} values for the Co and Co-alumina sample were respectively roughly 10 seconds versus 44 seconds.

After the incubation step, the analyzed Raman band would emerge and its intensity would increase exponentially. This corresponds to the acceleration growth phase shown in Figure 28(b). In terms of CNT growth, this is likely due to either the rapid initial lengthening of the CNTs at an exponential rate or the sudden exponential rise in

the number of activated catalytic nanoparticles that can produce CNTs. As we shall see, instead of directly measuring the duration of this phase, whose start and end times can be difficult to define, we extract a more meaningful characteristic time constant (i.e. τ_{acc}), by analyzing the results of an exponential fit.

After some time, the signal intensity increase would slow down and stabilize to a steady, linear growth phase, likely associated with steady CNT lengthening. This is the linear growth phase, indicated in Figure 28(c). Depending on its duration, the linear phase may not exist as a distinct, well defined step, but rather a transition between the exponential growth and eventual intensity saturation of the CNT sample. Regardless, as with the incubation step, its duration (i.e. t_{lin}) is directly measured for each analyzed band on the Co samples. While linear growth can be observed on several low temperature Co-alumina samples, due to the aforementioned spectral background fluctuations, its duration in these cases is not clearly defined. Otherwise, on other higher temperature Co-alumina samples, the end of the linear phase cannot be measured due the overall slow down in growth.

Finally, the termination phase, shown in Figure 28(d), would commence, causing the signal intensity growth rate to decelerate and eventually stop, thereby ending CNT growth. This step could not be clearly observed on the Co-alumina samples. Furthermore, among a few Co samples, complete growth saturation did not occur, but the Raman signal continued to grow at a very slow rate. Regardless, all analyzed Raman bands from the Co samples could have this final step exponentially fit, in a similar manner to the incubation step, allowing a characteristic time to be extracted (i.e. τ_{term}). CNT growth termination is often attributed to catalyst-poisoning phenomena.

The exponential fit of this final phase is consistent with the analysis performed in other kinetic CVD-CNT growth studies [6,8--10,70,71]. In forest-based, CVD studies, the phenomenon that we have described as the termination phase, that is, a gradual exponential decrease in CNT growth rates, will typically dominate CNT growth evolution curves. The first three phases we have detailed have been less frequently observed in prior studies. One reason for this may simply be the relatively low flow rates, along with the particular spectroscopic techniques and sampling rates used in this study. Regardless, one common form of analysis is to fit evolution curves to functions directly proportional to $\exp(-t/\tau_{term})$, where t is the growth time and $1/\tau_{term}$ effectively acts as a growth rate constant, based largely on the work of refs. [9,10]. In this study, we additionally perform an analogous fit to the acceleration phase data of each analyzed band, by fitting it to a function directly proportional to $\exp(+t/\tau_{inc})$, before extracting and tabulating the time constants.

It is unusual that Raman band emergence and overall growth rates across all samples are delayed with increasing temperature, since the rates of most chemical reactions will instead proceed faster as temperature is increased, as described by the well known empirical Arrhenius equation:

$$k = Ae^{\frac{-E}{k_B T}} \quad (7)$$

where k is the reaction rate, $E = E_a/N_A$ is the activation energy per molecule, k_B is the Boltzmann constant and T is the reaction temperature.

One explanation for our observations is that there is more than one reaction controlling the CNT growth rates. In the simplest scenario, two competing reactions

could be present. One reaction would be the dominant carbon-addition process that causes graphitic carbon to accumulate on each catalyst nanoparticles, thereby feeding CNT growth. This reaction may involve adsorption, migration or other chemical mechanisms. The other reaction would be the dominant carbon-removal process that hinders the addition of graphitic carbon from the nanoparticles, thereby preventing CNT growth. For example, this might involve the premature removal of gas phase carbon from the reactor or the desorption/diffusion of carbon molecules previously accumulated on the nanoparticles. While the rates of both reactions would increase with temperature, one feasible scenario is that the rate of the carbon-removal process would increase faster than the carbon-addition process, resulting is a net decrease in overall growth rates and times. Alternatively, some altogether different competing process, such as catalyst poisoning, might only become important at high temperatures.

Whatever the cause, it is more common for other studies to show an increase in CNT growth rates with increasing temperature. There are exceptions; for example, *in situ* Raman studies by Picher *et al.* also show a similar rate slow down for Co catalyst. [8] This phenomenon might be related to the use of relatively low flow rates in this study, while other studies will frequently use ~10-100 times the amount of gas flow.

We now fully discuss how the characteristic times of t_{inc}, τ_{acc}, t_{lin} and τ_{term}, which define the Raman band growth rates, increase with temperature. The inverses of these constants effectively represent reaction rates. As shown in Figure 29, all tabulated time constants are plotted against inverse temperature on natural log scales for the kinetic G bands of both the Co and Co-alumina samples (shown respectively as solid and crossed squares). Overall, the Co-alumina time constants are larger than those of the

corresponding Co sample values. Because of the 5 second sampling rate of the kinetic Co spectra, any corresponding low temperature t_{inc} values measured beneath this time are not meaningful. No Co t_{lin} values were measured below 5s and no Co-alumina t_{inc} and t_{lin} values were measured below their 0.7s sampling rate.

Note that in Figure 29, the error bars of the incubation and linear t parameters correspond to the uncertainty in the length of the incubation/linear time stages that are measured directly from the evolution curves. The error bars of the acceleration and termination τ parameters correspond instead to the error obtained from the algorithm used to fit the exponential acceleration and termination stages.

Only G band data is presented Figure 29, but additional D and RBM band data is presented in Appendix F. The Co sample RBM-1 characteristic times generally closely agreed with the G band times, while most Co sample RBM-2 and D signals were too weak to obtain accurate time constants. Likewise, all available τ_{acc} values from the G and D bands on the Co-alumina samples agreed, as did with those t_{inc} values below 750°C. However, it remains unclear whether the Co-alumina D band t_{inc} values above 750°C lag behind those of the G band or whether the spectral signal can be meaningfully analyzed above this temperature.

Linear trend-lines in Figure 29 (in red) have been fitted to the time constants of the two sample-types. A possible inflection point splits the trend-lines of the Co-alumina t_{inc} constants at roughly 775°C, similar to the sudden sharp increase in t_{inc} values experienced by Co samples above the same temperature. This may indicate that a common incubation-inhibition process becomes active at 775-825°C for both sample types. In an *in situ* optical study of forest growth using a similar catalyst formulation, a

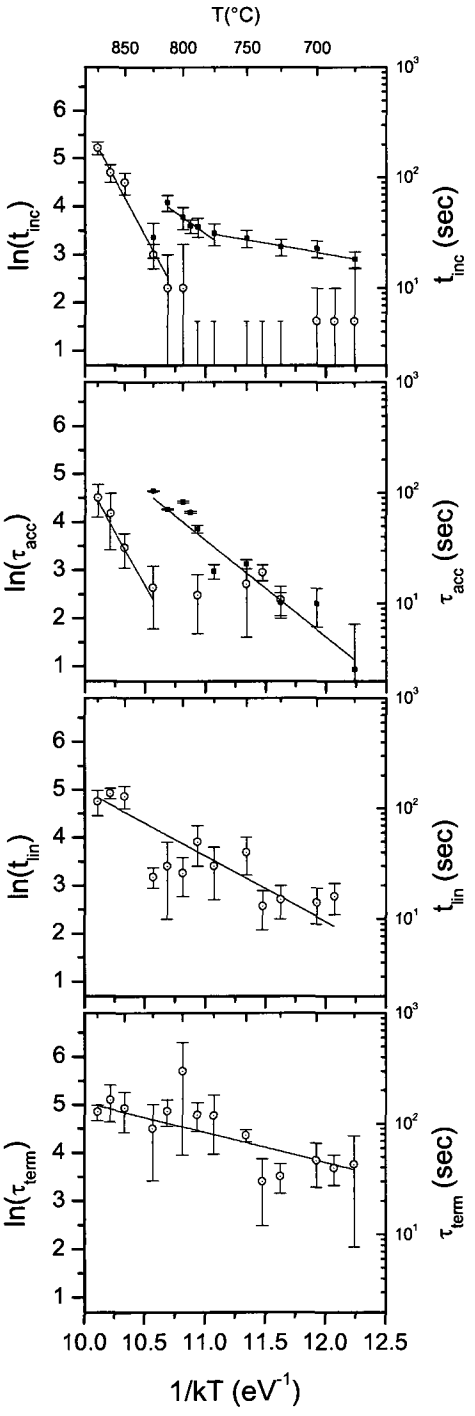

Figure 29: Characteristic energy plots of the Co and Co-alumina time constants: (a) incubation time; (b) accelerating time; (c) linear time; (d) termination time. Co-alumina linear and termination time constants could not be obtained. Characteristic times from the integrated G band intensities for the Co samples (empty circles) and Co alumina samples (filled boxed) are plotted. Characteristic energies correspond to the slope of the linear plots (red lines). From ref. [65].

similar critical point was observed in terms of temperature dependent forest height, growth rate and termination rate. [70] The same mechanism might therefore be present in this study. Alternatively, particularly in the case of the Co data, the split may simply be an artifact of noise. In terms of other time constant trends, the Co τ_{acc} values sharply increase above 825°C, while the Co-alumina τ_{acc} maintain a fairly steady relationship across all growth temperatures. In order words, a possible inflection point for the Co τ_{acc} data may be present between 775-825°C, but does not appear in the Co-alumina τ_{acc} data, although a subtle in the 775°C Co-alumina τ_{acc} data point is visible. The Co sample t_{lin} and τ_{term} values have larger uncertainties because the associated growth stages are more difficult to measure/fit, but they too both tend to increase at larger temperatures.

The slopes of these lines correspond to energy values in eV. If the slopes were of the opposite sign, their magnitudes could be interpreted as activation energies for CNT growth. [72] Instead, we refer to these slope values as "characteristic energies", which might correspond to net energy parameters resulting by one or more competing processes, which can still be used to quantify reaction rates. While the absolute value of these energies may not be clearly meaningful, their relative magnitudes are useful for comparing the growth rates between different sets of samples.

We again highlight the fact that the t_{inc} and τ_{acc} values are significantly different for the two sample types and that the alumina support likely plays an active role in determining initial CNT growth rates. Although CNT yield is significantly higher for the Co-alumina samples versus the Co samples, the Co-alumina t_{inc} and τ_{acc} values are still

higher than their Co counterparts, perhaps suggesting that surface or bulk diffusion processes interacting directly with the catalyst support are the differentiating factors. It follows that the presence of such diffusion processes would also play a determining role in whether either surface or forest growth is triggered.

The tabulated characteristic energies from the trend-lines of Figure 29 are presented in Table 1 for each sample type and growth stage. Larger characteristic

Growth stage:	Characteristic energy for Co samples:	Characteristic energy for Co-alumina samples:
Incubation	4.7eV ± 0.8eV*	1.8eV ± 0.6eV† and 0.4eV ± 0.2eV§
Acceleration	4eV ± 1eV‡	2.0eV ± 0.4eV
Linear growth	1.4eV ± 0.6eV	----
Termination	0.6eV ± 0.5eV	----

* 800°C-875°C, † 775°C-875°C, § 675°C-775°C, ‡825°C-875°C

Table 1: Characteristic energies associated with each stage of growth and sample type.

energies indicate a greater decrease in CNT growth rate with increasing temperature. The high temperature characteristic energies for the Co incubation and acceleration stages agree to within experimental uncertainty, suggesting that they are the result of a common process. Likewise, the high temperature characteristic energies for the Co-alumina incubation and acceleration also agree, although they are also at lower values that those of the Co sample.

It is therefore possible that the same carbon removal process occurs on both samples, but that the presence of the alumina support modulates the net growth process, somewhat mitigating the effects of temperature on early CNT growth. The carbon removal process could be due to an unwanted side reaction, such as pyrolysis of gas phase ethanol or a direct chemical reaction with the substrate. The presence of alumina, on the other hand, could simply increase the rate of the dominant carbon addition process at higher temperatures, thereby counteracting some effects of carbon removal. In a recent comprehensive CNT supergrowth study by Futaba *et al.*, the presence of controlled amounts of oxygen in different gaseous growth enhancers was shown to clean the catalyst nanoparticles of amorphous carbon, thereby prolonging growth. [73] Although the oxide in our support layer is solid, it may be possible that a similar cleaning effect is taking place, thereby promoting forest growth, but also affecting the amount of carbon interacting with the catalyst.

Finally, the fact that the Co sample linear and termination growth stages are significantly less sensitive to temperature than the initial growth stages, may indicate that the dominant growth termination process, possibly catalyst poisoning, is also less temperature dependent. The characteristic energies of these two final stages also agree, perhaps indicating that a common termination process is present and that linear growth can be seen as an early extension of termination growth.

We reemphasize that four-step growth process has precedence in other work, with the incubation and exponentially accelerating phases sometimes being observed. Very early studies by Baker *et al.* on the growth of filamentous carbon with metal catalysts revealed, through electron microscopy, qualitatively similar accelerating, linear, and

deceleration growth stages. [74,75] More contemporary *in situ* CVD-CNT forest growth studies, which monitor forest height evolution, show initial accelerating growth rates. These include the Fabry-Perot reflectivity studies of Puretzky *et al.* [9,71], the optical reflectivity interference studies of Kim *et al.* [76], and the work of Eres *et al.* [77]. Lin *et al.*'s study of SWNT length evolution using transmission electron microscopy showed both a delay prior to observable CNT growth (similar to incubation), in addition to accelerating growth. [78] Exponentially increasing CNT growth rates is also inferred from an *in situ* Raman study via blackbody measurements [79], an x-ray spectroscopy study [33], work involving *in situ* SEM [80], and a study measuring catalyst weight gain [81]. Additionally, past *in situ* GRI studies for CVD-CNT growth at IMS-NRC also showed accelerating, linear, and prolonged termination phases when the integrated image intensity was tracked. [54]

Linear and termination growth stages, without visible incubation and accelerating phases are also observed in a number of *in situ* optical studies that monitor forest height. In addition to previously mentioned work, optical absorbance work by Einarsson *et al.* using an ethanol-CVD setup observed and fitted exponentially decaying termination rates at different growth temperatures and found that pressure determined the dominant rate-limiting reaction. [82] Different water-enhanced, "supergrowth" studies, using a variety of reactants, also reveal forests that exhibit exponential decay rates during termination. [10,31,83] Perhaps more relevant to the current work, the *in situ* Raman G band tracking study in Picher *et al.* too shows exponential decay. If growth proceeds too quickly or if the optical monitoring requires a minimum forest height for detection, it is possible to miss the accelerating phase, should it be present. Exponential rate decay does not always

occur however, and abrupt termination is also possible. [84--87] In our study, no growth data beyond the accelerating phase in the Co-alumina samples could be analyzed, so forest termination rates could not be assessed.

In future work, it would be interesting to establish how process dependent the observed growth trends are, particularly the overall growth slowdown with increased growth temperature. To better understand the growth difference on the Co versus the Co-alumina samples, differences in catalytic nanoparticle size and shape could be studied. Repeating the experiment using a different reactor and gas system may also be worthwhile, in order to determine how dependent growth is on the specific reactor setup.

7. CONCLUSIONS

To summarize, using *in situ* Raman spectroscopy, we have successfully monitored the growth rates of different Raman bands related to CNT presence during CVD synthesis. Four distinct growth steps, namely incubation, acceleration, linear and termination phases, were found to occur during signal evolution across all analyzed G, D and RBM signals. Higher sampling rates and signal intensities are required to conclude whether the D band growth rates at higher growth temperatures lag behind the G band growth rates. Otherwise, the analyzed low temperature D bands and all the analyzed G and RBM bands on a given samples appeared to closely track together. The concurrent analysis of two distinct RBM peaks, in particular, provides evidence that the kinetic diameter distribution of growing SWNTs remains fairly constant under our CVD process and apparatus. The effect of temperature scaling on two types of substrate was studied by extracting parameterized time constants for each analyzable step, and plotting the natural logarithms of these time values against the inverse growth temperature. From these plots, characteristic energy values were then extracted and analyzed from the slopes of the approximately linear trend-lines. Increased temperature was found to reduce the overall rate of CNT growth on both studied sample types, although the presence of an alumina catalyst support would seem to reduce this temperature dependent rate reduction. A possible explanation for this is that there is a temperature activated process that interferes with the carbon accumulation on the catalytic nanoparticles that is necessary for CNT growth. At increasing temperatures, the rate of this interfering process may increase at a faster rate than the rate of carbon accumulation on the nanoparticles. Possible

mechanisms for this interference process include the burning of gas phase ethanol or carbon desorption from nanoparticle surface. The added presence of alumina would then presumably modulate the rate determining interference or accumulation reactions.

Appendix A: Growth method

The step-by-step process used to grow all samples is summarized:

- open the reactor and load the cleaved sample
- close the reactor and lock it in the translation stage; position the reactor and adjust optics
- start H_2/Ar (98%/2%) purge by opening two parallel, downstream rotameters to maximum flow (i.e. 76 sccm and 15 sccm)
- heat crucible to 200°C at 100°C/min (monitored by thermocouple), then hold purge for 20min
- heat crucible to growth temp.; all ramping below 800°C is done at 100°C/min; above 800°C, ramping is done at 25°C/min
- at growth temp., drop flow to 0 sccm and 2 sccm; hold for ~5min
- reroute flow through bubbler; bubble ethanol for a growth time of 20 minutes for "Co samples" or 5 minutes for "Co-alumina samples"
- after allotted time, immediately divert flow to bypass bubbler
- open rotameters to 76 sccm and 15 sccm; hold for ~5min to purge reactor
- ramp down to room temperature
- below 30°C, close both rotameters

During the process, Raman spectroscopy and Global Raman Imaging are performed on the samples before, during, and after growth.

Appendix B: Background subtraction method

As an example, Figure B1 illustrates background subtraction performed on the post-growth, 813°C grown Co sample for the high temperature RBM and G bands:

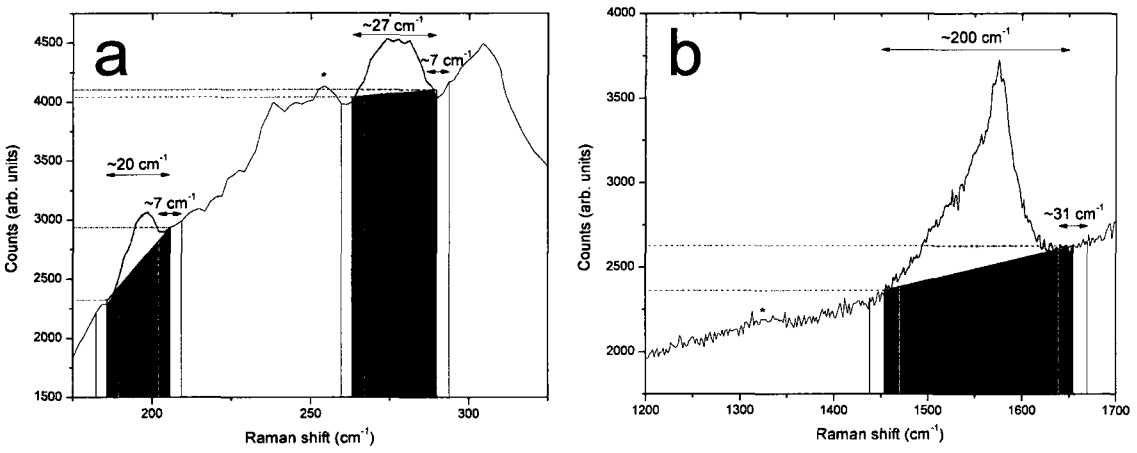

Figure B1: Background correction performed on the (a) RBM bands (namely "RBM-1" and "RBM-2") and the (b) G band of the post-growth, 813°C grown Co sample at growth temperature. Blue areas indicate the subtracted background, red areas indicate the extracted integrated area, and asterisks indicate bands too weak to extract. From ref. [65].

The same correction process was used for all analyzed Raman bands. After identifying a Raman band, its spectral width is first measured. The idea is to subtract the substrate-related background (in blue) from the total integrated area below the peak, leaving the corrected area (in red). To do this, averaged count values must be assigned to the endpoints to the left and the right of each band to account for noise. A vertical slice is therefore drawn about each endpoint; for the G and D bands the width of this slice is ~31 cm^{-1}, while the slice width for the RBM-1 and RBM-2 is 7 cm^{-1}. The averaged count values are then simply obtained by dividing the area of each slice with the slice width. A

straight line is drawn from each endpoint and the trapezoidal area below the line can be subtracted away. More intense Raman bands, with high signal/noise, are easier to correct for, while irregular, background features (such as the SiO_2 background from ~200-315 cm^{-1}) may interfere with the correction. As a result, for Raman peaks that emerge during CNT growth, the corrected Raman band area at t=0s is not always 0, so a small constant is often added or subtracted from the area values to correct for this.

Appendix C: Temperature dependency of Raman features

The intensity and Raman shift location of the certain Raman bands were found to be dependent on temperature. Figure C1 depicts the typical post-growth spectra for a 800°C grown Co sample, taken at different temperatures. No spectral changes were observed before room temperature and 200°C.

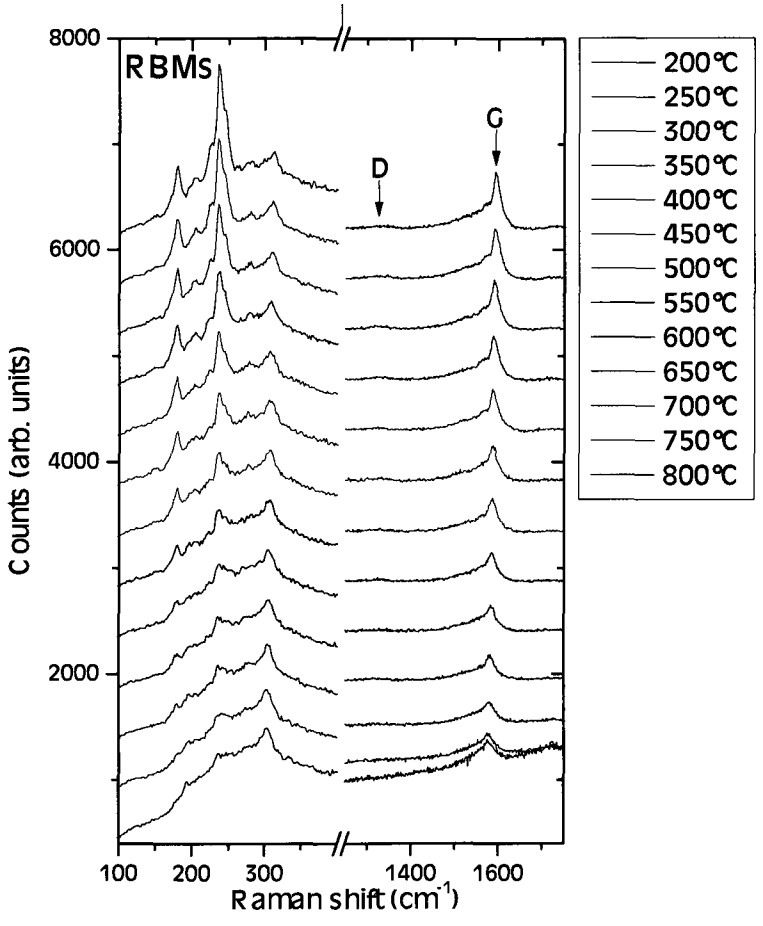

Figure C1: Temperature dependent Raman spectra for a Co sample grown at 800°C. From ref. [65].

The intensity of RBM peaks at room temperature is greatly reduced at higher temperatures. Conversely, certain RBM peaks became more intense at higher temperature. The analyzed RBM-1 (at ~197 cm^{-1}) and RBM-2 (at ~277 cm^{-1}) peaks in particular vanish below ~650°C and became more intense above this temperature. As described by Uchida *et al.*, these intensity changes are due to the temperature dependence of the RBM resonance conditions. [88] Many more RBM peaks were present at low temperature than at high temperature, for all samples with room temperature RBMs. Studies, such as those in references [88] and [89], also explain the observed slight downshift in RBM peak location of up to ~3 cm^{-1} at increasing temperature. The temperature dependency of factors such as C-C bond structure and van der Waals interactions between CNTs may have important roles. [89]

On both the Co and Co-alumina samples, the integrated G and D band intensities are relatively stable across all temperatures, although both bands become sharper at lower temperatures. The G+ and G- are more distinct at lower temperatures. The I_D/I_G ratio on a given sample also remains fairly stable at different temperature. Finally, the G and D bands also experience downshifting with increasing temperature, of up to ~20 cm^{-1} and ~15 cm^{-1} respectively.

Appendix D: Raman area traces for all grown samples

The growth evolution Raman area traces for the Co and Co-alumina samples are presented as waterfall plots at different growth temperatures. Figures D1-D4 show the evolution curves of the Co sample G, D, RBM-1, and RBM-2 bands, respectively. Figures D5-D6 show the evolution curves of the Co-alumina sample G and D bands, respectively. All evolution curves are background corrected. Intermittent spikes in intensity correspond to cosmic ray events.

While G band data was available for both samples over all growth temperatures, certain Raman bands were too weak to track meaningfully and were not plotted. Also, due to excessive growth in the Co-alumina samples, the G and D traces are only accurate during their incubation and acceleration phases. For example, the sudden rise or dip in G band signal after ~2-3 minutes of growth for Co-alumina samples grown below 800°C is related to film opacity and should be disregarded.

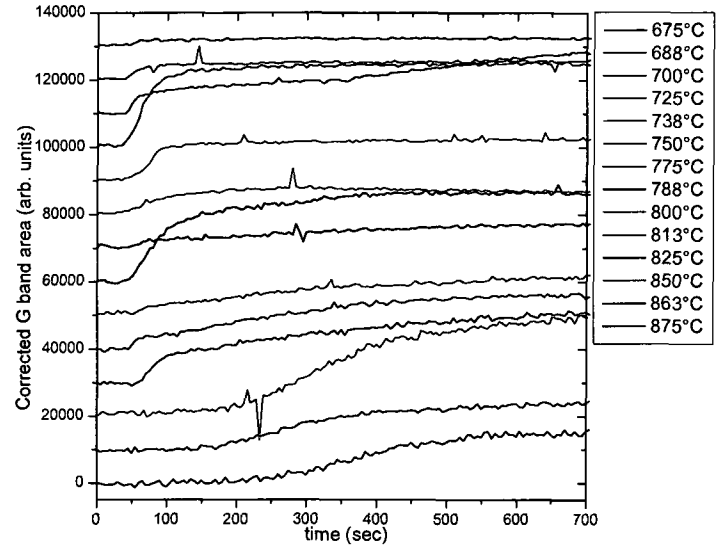

Figure D1: Time evolution of the integrated G band of Co samples grown at different temperatures. A 4.5s exposure time was used for the 850°C grown Co sample, instead of the usual 5s due to error. From ref. [65].

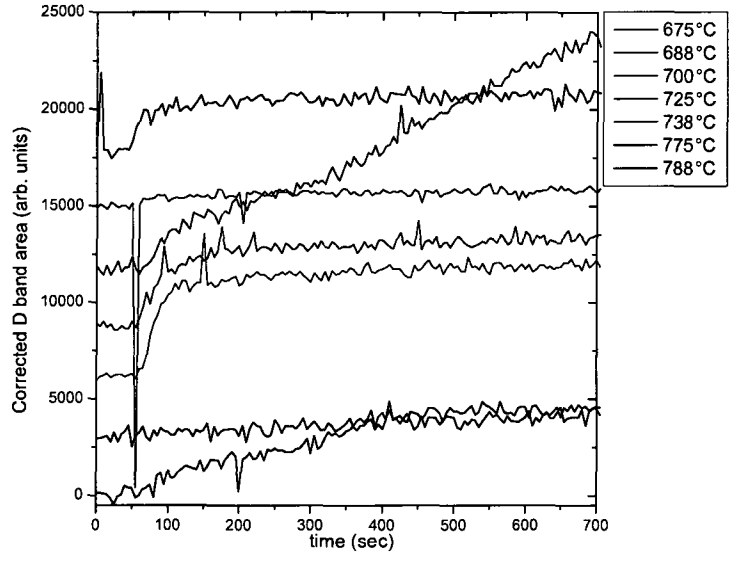

Figure D2: Time evolution of the integrated D band of Co samples grown at different temperatures. From ref. [65].

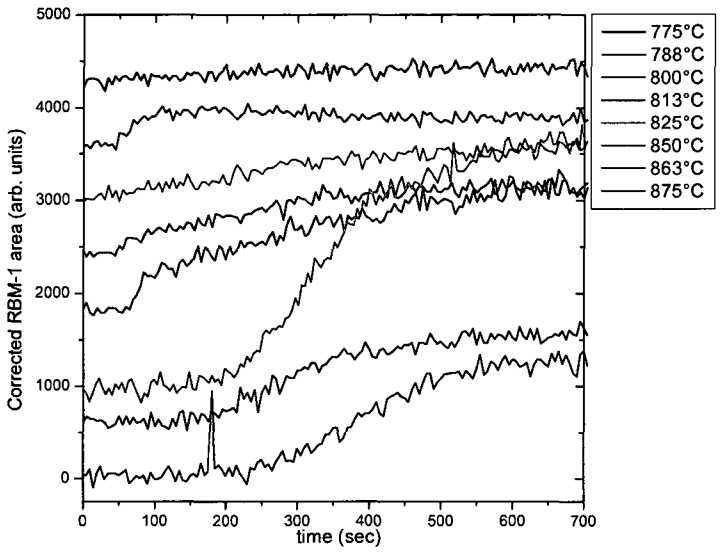

Figure D3: Time evolution of the integrated RBM-1 band of Co samples grown at different temperatures. From ref. [65].

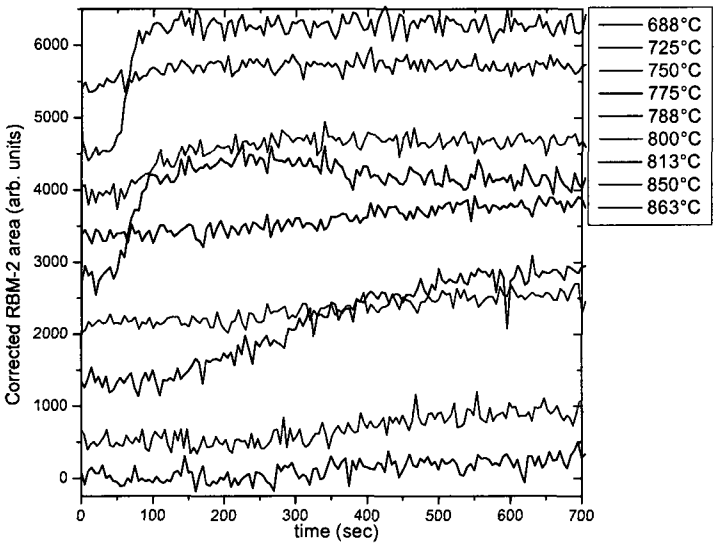

Figure D4: Time evolution of the integrated RBM-2 band of Co samples grown at different temperatures. From ref. [65].

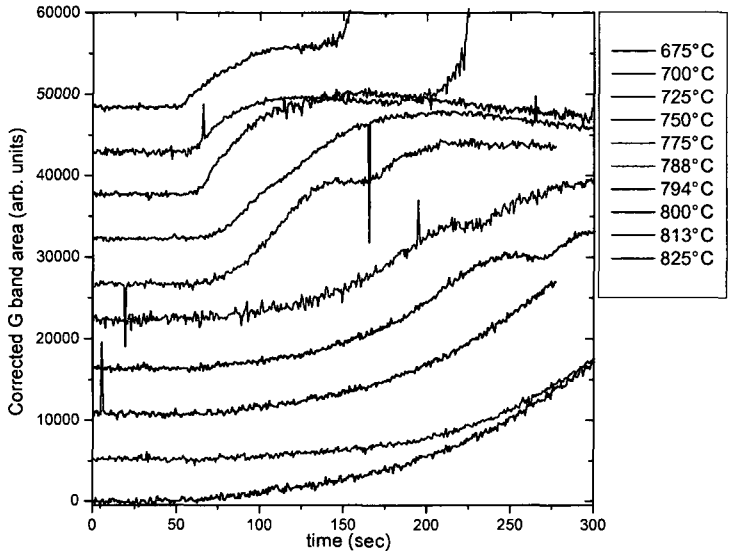

Figure D5: Time evolution of the integrated G band of Co-alumina samples grown at different temperatures. Samples grown at 775°C and 800°C were grown for ~4min, 30sec prior to growth being standardized to 5min. From ref. [65].

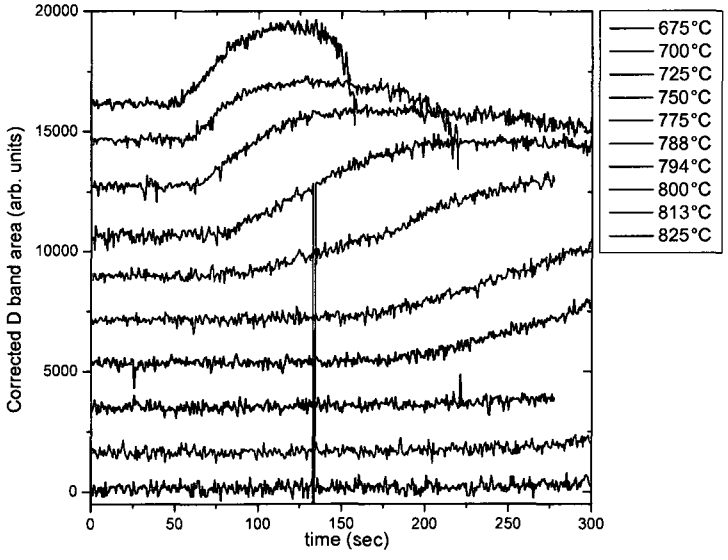

Figure D6: Time evolution of the integrated D band of Co-alumina samples grown at different temperatures. The 675°C and 700°C evolution plots have been clipped at large time values. From ref. [65].

Appendix E: Room temperature I_D/I_G ratios

Ratios of D and G band intensities are frequently used in Raman studies to assess the crystallinity and quality of CNT samples. Figure E1 depicts the post-growth I_D/I_G ratios of the Co and Co-alumina samples at room temperature, grown at different temperatures.

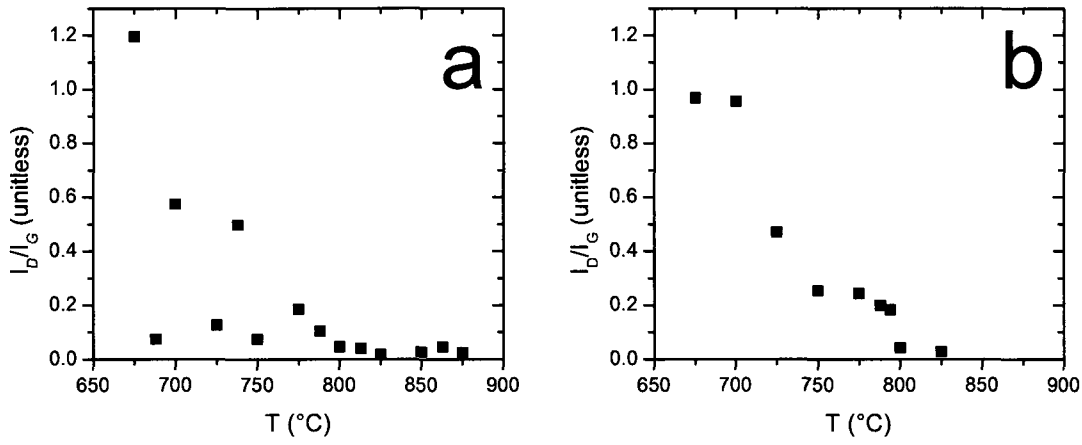

Figure E1: The room temperature I_D/I_G plots for the post-growth (a) Co and (b) Co-alumina samples.

The I_D/I_G values were found to decrease for both sample types with increasing temperatures, indicating increased CNT crystallinity at higher temperatures, as expected. Post-growth G and D intensities were difficult to obtain for the Co-alumina samples grown at 675°C and 700°C due to the very broad spectral backgrounds that were present. These intensities were obtained from particular regions on each sample where background signal was at a minimum.

Appendix F: Characteristic energy plots with additional RBM-1 and D band data

Figure F1 depicts the G band characteristic times previously presented in Figure 29, with the addition of characteristic times from the Co samples' RBM-1 bands and from the Co-alumina samples' D bands. Many of the Co samples' RBM-2 integrated intensities are too weak to extract time constants, so these were not plotted. Similarly, only the incubation times of the RBM-1 bands could be accurately extracted, due to their low signals.

The incubation times of the Co sample RBM-1 bands are almost the same as those of the G band. The shown incubation characteristic energy (i.e. 4eV ± 1eV) is calculated using both the G and D bands and was found to agree with the energy calculated using only the G band, given in Table 1. Below 775°C, the RBM-1 incubation time falls below the 5s sampling rate.

The Co-alumina D band incubation times match less well with their corresponding G band values, especially above 750°C. However, at these higher temperatures the D band intensity is extremely low, and it is possible that the D bands emerge earlier than indicated, but do so below the signal/noise threshold and cannot be directly observed. Due to the large uncertainty of these values, an associated characteristic energy was not plotted.

The Co-alumina D band acceleration times match closely with those of the G band. The shown characteristic energy (i.e. 2.2eV ± 0.4eV) was re-plotted using both the G and D band data, and was also found to agree with the G band only energy listed in Table 1.

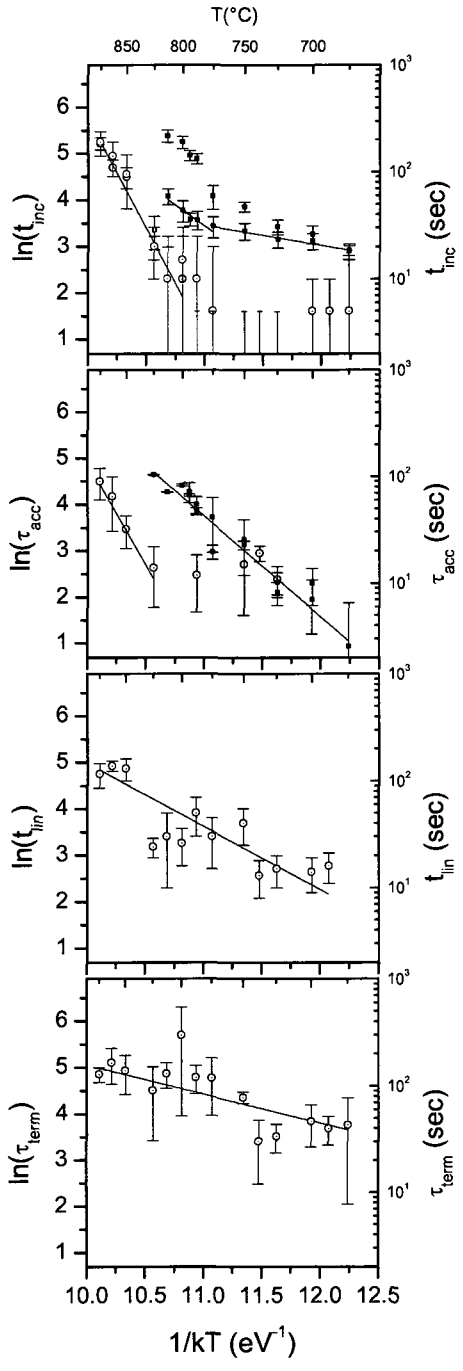

Figure F1: Characteristic energy plots of the Co and Co-alumina time constants: (a) incubation time; (b) accelerating time; (c) linear time; (d) termination time. Co-alumina linear and termination time constants could not be obtained. Characteristic times from the integrated RBM-1 band intensities for the Co samples (empty orange circles) and from the integrated D band intensities for Co alumina (filled violet boxes) samples are plotted, in addition to those of the G band from the Co samples (empty circles) and Co-alumina samples (filled black boxes). Characteristic energies correspond to the slope of the linear plots (red lines). From ref. [65].

ACKNOWLEDGEMENTS

A grant from Le Fonds québécois de la recherche sur la nature et les technologies (FQRNT) and a discovery grant from Natural Sciences and Engineering Research Council of Canada (NSERC) are gratefully acknowledged. Thanks to Paul Finnie, Paul Marshall, Hue Tran, Kate Kaminska, Jacques Lefebvre, Jeff Fraser, Phillip Vinten, and Jeffery Bond for assistance and preliminary work. Thanks to Javier Giorgi, Michel Godin, and Kevin Graham for their useful thesis defense commentary. We are grateful for the funding of *in situ* Raman studies via the former JST-CREST "Nanofactory" project led by Yoshikazu Homma.

REFERENCES

[1] S. Iijima, Nature **354**, 56 (1991).

[2] A. Zettl, *Carbon nanotubes : quantum cylinders of graphene, Chapter 1 - NANOTUBES: AN EXPERIMENTAL OVERVIEW* (Elsevier, Amsterdam, 2008), p. 1.

[3] E. T. Thostenson, Z. Ren, and T. Chou, Composites Sci. Technol. **61**, 1899 (2001).

[4] F. Hennrich, C. Chan, V. Moore, M. Rolandi, and M. J. O'Connell, *Carbon Nanotubes : Properties and Applications, Chapter 1 - The element carbon* (CRC/Taylor & Francis, Boca Raton, FL, 2006.), p. 1.

[5] B. L. Allen, P. D. Kichambare, and A. Star, Adv Mater **19**, 1439 (2007).

[6] S. Chiashi, Y. Murakami, Y. Miyauchi, and S. Maruyama, Chemical Physics Letters **386**, 89 (2004).

[7] S. Dittmer, N. Olofsson, J. Ek Weis, O. A. Nerushev, A. V. Gromov, and E. E. B. Campbell, Chemical Physics Letters **457**, 206 (2008).

[8] M. Picher, E. Anglaret, R. Arenal, and V. Jourdain, Nano Letters **9**, 542 (2009).

[9] A. A. Puretzky, D. B. Geohegan, S. Jesse, I. N. Ivanov, and G. Eres, Appl. Phys. A **81**, 223 (2005).

[10] D. N. Futaba, K. Hata, T. Yamada, K. Mizuno, M. Yumura, and S. Iijima, Phys. Rev. Lett. **95**, 056104 (2005).

[11] S. Saito, *Carbon nanotubes : quantum cylinders of graphene, Chapter 2 - QUANTUM THEORIES FOR CARBON NANOTUBES* (Elsevier, Amsterdam, 2008), p. 29.

[12] W. Kim, H. C. Choi, M. Shim, Y. Li, D. Wang, and H. Dai, Nano Letters **2**, 703 (2002).

[13] R. V. Seidel, A. P. Graham, B. Rajasekharan, E. Unger, M. Liebau, G. S. Duesberg, F. Kreupl, and W. Hoenlein, J. Appl. Phys. **96**, 6694 (2004).

[14] P. Finnie, A. Li-Pook-Than, J. Lefebvre, and D. G. Austing, Carbon **44**, 3199 (2006).

[15] D. Mann, *Carbon Nanotubes: Properties and Applications, Chapter 2 - Synthesis of carbon nanotubes* (CRC/Taylor & Francis, Boca Raton, FL, 2006), p. 19.

[16] A. Jorio, M. A. Pimenta, A. G. S. Filho, R. Saito, G. Dresselhaus, and M. S. Dresselhaus, New Journal of Physics **5**, 139 (2003).

[17] P. G. Collins and P. Avouris, *Carbon nanotubes : quantum cylinders of graphene, Chapter 3 - THE ELECTRONIC PROPERTIES OF CARBON NANOTUBES* (Elsevier, Amsterdam, 2008), p. 49.

[18] P. McEuen and C. Kittel, *Nanostructures* (Wiley, Hoboken, NJ;, 2005), p. 515.

[19] M. S. Dresselhaus, G. Dresselhaus, R. Saito, and A. Jorio, *Carbon nanotubes : quantum cylinders of graphene, Chapter 4 - RAMAN SPECTROSCOPY OF CARBON NANOTUBES* (Elsevier, Amsterdam, 2008), p. 83.

[20] T. Ando, J.Phys.Soc.Jpn. **74**, 777 (2005).

[21] M. S. Dresselhaus, G. Dresselhaus, R. Saito, and A. Jorio, Physics Reports **409**, 47 (2005).

[22] K. Harigaya, Phys. Rev. B **60**, 1452 (1999).

[23] C. D. Spataru, S. Ismail-Beigi, L. X. Benedict, and S. G. Louie, Phys. Rev. Lett. **92**, 077402 (2004).

[24] G. Dukovic, F. Wang, D. Song, M. Y. Sfeir, T. F. Heinz, and L. E. Brus, Nano Letters **5**, 2314 (2005).

[25] R. Martel, T. Schmidt, H. R. Shea, T. Hertel, and P. Avouris, Appl. Phys. Lett. **73**, 2447 (1998).

[26] S. K. Doorn, D. Heller, M. Usrey, P. Barone, and M. S. Strano, *Carbon Nanotubes: Properties and Applications, Chapter 6 - Raman spectroscopy of single-walled carbon nanotubes: probing electronic and chemical behavior* (CRC/Taylor & Francis, Boca Raton, FL, 2006), p. 153.

[27] K. Y. Shin, C. T. Lee, J. S. Kao, C. C. Kei, C. M. Chang, C. N. Hsiao, J. H. Liang, K. C. Leou, and C. H. Tsai, J. Vac. Sci. Technol. B **25**, 1842 (2007).

[28] E. Joselevich, H. Dai, J. Liu, K. Hata, and A. H. Windle, *Carbon Nanotube Synthesis and Organization*, 2008), p. 101.

[29] S. P. Patole, P. S. Alegaonkar, H. Shin, and J. Yoo, J. Phys. D **41**, 155311 (2008).

[30] K. Hata, D. N. Futaba, K. Mizuno, T. Namai, M. Yumura, and S. Iijima, Science **306**, 1362 (2004).

[31] H. Ago, N. Uehara, N. Yoshihara, M. Tsuji, M. Yumura, N. Tomonaga, and T. Setoguchi, Carbon **44**, 2912 (2006).

[32] S. Noda, K. Hasegawa, H. Sugime, K. Kakehi, Z. Zhang, S. Maruyama, and Y. Yamaguchi, Jpn. J. Appl. Phys. **46**, L399.

[33] C. Mattevi, C. T. Wirth, S. Hofmann, *et al*, The Journal of Physical Chemistry C **112**, 12207 (2008).

[34] D. P. Burt, W. M. Whyte, J. M. R. Weaver, A. Glidle, J. P. Edgeworth, J. V. Macpherson, and P. S. Dobson, The Journal of Physical Chemistry C **113**, 15133 (2009).

[35] Y. Li, W. Kim, Y. Zhang, M. Rolandi, D. Wang, and H. Dai, The Journal of Physical Chemistry B **105**, 11424 (2001).

[36] C. L. Cheung, A. Kurtz, H. Park, and C. M. Lieber, The Journal of Physical Chemistry B **106**, 2429 (2002).

[37] A. G. Nasibulin, P. V. Pikhitsa, H. Jiang, and E. I. Kauppinen, Carbon **43**, 2251 (2005).

[38] W. Zhou, L. Ding, and J. Liu, Nano Research **2**, 593 (2009).

[39] S. Sato, A. Kawabata, M. Nihei, and Y. Awano, Chemical Physics Letters **382**, 361 (2003).

[40] S. Esconjauregui, C. M. Whelan, and K. Maex, Carbon **47**, 659 (2009).

[41] N. Geblinger, A. Ismach, and E. Joselevich, Nat Nano **3**, 195 (2008).

[42] Y. Homma, Y. Kobayashi, T. Ogino, D. Takagi, R. Ito, Y. J. Jung, and P. M. Ajayan, The Journal of Physical Chemistry B **107**, 12161 (2003).

[43] R. W. Boyd, *Nonlinear optics, Chapter 10: Stimulated Raman Scattering and Stimulated Rayleigh-Wing Scattering* (Academic Press, New York, 2003), p. 451.

[44] A. Jorio, E. Kauppinen, and A. Hassanien, *Carbon-Nanotube Metrology* (Springer, New York, 2008), p. 63.

[45] X. Zhao, Y. Ando, L. Qin, H. Kataura, Y. Maniwa, and R. Saito, Chemical Physics Letters **361**, 169 (2002).

[46] R. B. Weisman and S. M. Bachilo, Nano Letters **3**, 1235 (2003).

[47] M. S. Strano, J. Am. Chem. Soc. **125**, 16148 (2003).

[48] H. Telg, J. Maultzsch, S. Reich, F. Hennrich, and C. Thomsen, Phys. Rev. Lett. **93**, 177401 (2004).

[49] Y. Murakami, Y. Miyauchi, S. Chiashi, and S. Maruyama, Chemical Physics Letters **377**, 49 (2003).

[50] R. Saito, G. Dresselhaus, and M. S. Dresselhaus, Phys. Rev. B **61**, 2981 (2000).

[51] H. Kataura, Y. Kumazawa, Y. Maniwa, I. Umezu, S. Suzuki, Y. Ohtsuka, and Y. Achiba, Synth Met **103**, 2555 (1999).

[52] S. Maruyama, *Kataura plot by S. Maruyama* (The University of Tokyo, Department of Mechanical Engineering, Maruyama-Shiomi Laboratory, 2002), Accessed Dec. 2009, http://www.photon.t.u-tokyo.ac.jp/~maruyama/kataura/kataura.html.

[53] K. Kaminska, J. Lefebvre, D. G. Austing, and P. Finnie, Phys. Rev. B **73**, 235410 (2006).

[54] K. Kaminska, J. Lefebvre, D. G. Austing, and P. Finnie, Nanotechnology **18**, 165707 (2007).

[55] Y. Kobayashi, T. Yamashita, Y. Ueno, O. Niwa, Y. Homma, and T. Ogino, Chemical Physics Letters **386**, 153 (2004).

[56] H. Son, Y. Hori, S. G. Chou, D. Nezich, G. G. Samsonidze, G. Dresselhaus, M. S. Dresselhaus, and E. B. Barros, Appl. Phys. Lett. **85**, 4744 (2004).

[57] P. Finnie, A. Li-Pook-Than, and J. Lefebvre, Nano Res **2**, 783 (2009).

[58] JEOL Ltd., *Scanning Electron Microscope A to Z: Basic Knowledge For Using The SEM* (JEOL Ltd USA, Inc., Online, 2009).

[59] A. Vijayaraghavan, C. W. Marquardt, S. Dehm, F. Hennrich, and R. Krupke, Carbon **48**, 494 (2010).

[60] T. Brintlinger, Y. Chen, T. Durkop, E. Cobas, M. S. Fuhrer, J. D. Barry, and J. Melngailis, Appl. Phys. Lett. **81**, 2454 (2002).

[61] R. Y. Zhang, Y. Wei, L. A. Nagahara, I. Amlani, and R. K. Tsui, Nanotechnology **17**, 272 (2006).

[62] Y. Homma, S. Suzuki, Y. Kobayashi, M. Nagase, and D. Takagi, Appl. Phys. Lett. **84**, 1750 (2004).

[63] P. Finnie, K. Kaminska, Y. Homma, D. G. Austing, and J. Lefebvre, Nanotechnology **19**, 335202 (2008).

[64] M. Suzuki, Y. Ominami, Q. Ngo, C. Y. Yang, T. Yamada, A. M. Cassell, and J. Li, J. Appl. Phys. **100**, 104305 (2006).

[65] A. Li-Pook-Than, J. Lefebvre, and P. Finnie, J. Phys. Chem. C (To be published 2010).

[66] A. Jorio, R. Saito, J. H. Hafner, C. M. Lieber, M. Hunter, T. McClure, G. Dresselhaus, and M. S. Dresselhaus, Phys. Rev. Lett. **86**, 1118 (2001).

[67] Y. Miyauchi, S. Chiashi, Y. Murakami, Y. Hayashida, and S. Maruyama, Chemical Physics Letters **387**, 198 (2004).

[68] H. E. Unalan and M. Chhowalla, Nanotechnology **16**, 2153 (2005).

[69] Y. Yao, X. Dai, R. Liu, J. Zhang, and Z. Liu, The Journal of Physical Chemistry C **113**, 13051 (2009).

[70] P. Vinten, J. Lefebvre, and P. Finnie, Chemical Physics Letters **469**, 293 (2009).

[71] A. A. Puretzky, G. Eres, C. M. Rouleau, I. N. Ivanov, and D. B. Geohegan, Nanotechnology **19**, 055605 (2008).

[72] J. L. MUENCH, J. KRUUV, and J. R. LEPOCK, Cryobiology **33**, 253 (1996).

[73] D. Futaba, J. Goto, S. Yasuda, T. Yamada, M. Yumura, and K. Hata, Advanced Materials **21**, 4811 (2009).

[74] R. T. K. Baker, M. A. Barber, P. S. Harris, F. S. Feates, and R. J. Waite, Journal of Catalysis **26**, 51 (1972).

[75] R. T. K. Baker, P. S. Harris, R. B. Thomas, and R. J. Waite, Journal of Catalysis **30**, 86 (1973).

[76] D. Kim, H. Jang, C. Kim, D. Cho, H. Yang, H. Kang, B. Min, and H. Lee, Nano Letters **3**, 863 (2003).

[77] G. Eres, C. M. Rouleau, M. Yoon, A. A. Puretzky, J. J. Jackson, and D. B. Geohegan, The Journal of Physical Chemistry C **113**, 15484 (2009).

[78] M. Lin, J. P. Ying Tan, C. Boothroyd, K. P. Loh, E. S. Tok, and Y. Foo, Nano Letters **6**, 449 (2006).

[79] S. Dittmer, N. Olofsson, J. Ek Weis, O. A. Nerushev, A. V. Gromov, and E. E. B. Campbell, Chemical Physics Letters **457**, 206 (2008).

[80] I. Wako, T. Chokan, D. Takagi, S. Chiashi, and Y. Homma, Chemical Physics Letters **449**, 309 (2007).

[81] A. Maroto Valiente, P. Navarro López, I. Rodrφguez Ramos, A. Guerrero Ruiz, C. Li, and Q. c. Xin, Carbon **38**, 2003 (2000).

[82] E. Einarsson, Y. Murakami, M. Kadowaki, and S. Maruyama, Carbon **46**, 923 (2008).

[83] S. Yasuda, D. N. Futaba, T. Yamada, J. Satou, A. Shibuya, H. Takai, K. Arakawa, M. Yumura, and K. Hata, ACS Nano **3**, 4164 (2009).

[84] A. A. Puretzky, G. Eres, C. M. Rouleau, I. N. Ivanov, and D. B. Geohegan, Nanotechnology **19**, 055605 (2008).

[85] P. Vinten, P. Marshall, J. Lefebvre, and P. Finnie, Nanotechnology **21**, 035603 (2010).

[86] E. R. Meshot and A. J. Hart, Appl. Phys. Lett. **92**, 113107 (2008).

[87] K. Hasegawa, S. Noda, and Y. Yamaguchi, Ninth International Conference on the Science and Applications of Nanotubes, NT08, T 23 (2008).

[88] T. Uchida, M. Tazawa, H. Sakai, A. Yamazaki, and Y. Kobayashi, Appl. Surf. Sci. **254**, 7591 (2008).

[89] N. R. Raravikar, P. Keblinski, A. M. Rao, M. S. Dresselhaus, L. S. Schadler, and P. M. Ajayan, Phys. Rev. B **66**, 235424 (2002).